A potential classification method for Motor Neuron Disease (MND) Using Hyperspectral Imaging (HSI) Technique

By

Meng He

Department of Physics and Astronomy

Supervisors:

Prof. Michael Steel

Prof. Ewa Goldys

Prof. Roger Chung

Dr. Annemarie Nadort

Dr. Wei Deng

MACQUARIE University
SYDNEY·AUSTRALIA

FACULTY OF SCIENCE AND ENGINEERING

This thesis is presented for the degree of Master of Philosophy

November 2019

I certify that the work in this thesis has not previously been submitted for a degree nor has it been submitted as part of requirements for a degree to any other university or institution other than Macquarie University.

I also certify that the thesis is an original piece of research, and it was authored by myself. Help and assistance that I have received in the course of my research work and in the preparation of the thesis itself have where appropriate, been acknowledged.

In addition, I certify that all information sources and literature used in the course of this research is also indicated where appropriate in this record of my thesis.

Meng He 21-Nov-2019

Acknowledgment

This project, which was like a rollercoaster, it has up and downs, and there are times that I wanted to quit, but I am glad that I finished this journey. However, it is impossible to complete this thesis without all the help that I got from everyone had supported me.

To begin, I need to thank my supervisor Professor Ewa Goldys, who has broadened my horizons, introduced me to the new world of hyperspectral imaging, and allowed me to work with her fantastic team of researchers in Macquarie University. I want to thank Ewa for guiding me into the demanding area of modern cross-disciplinary studies.

I am thankful to my acting supervisor Professor Michael Steel, who guides me through the last year of the research. He taught me how to present the results more scientifically and helped me to deliver the result on time. He reminds me how critical thinking can help me have more insight into my project and produce a better result. I am very thankful to you for trusting me, even when I was not in my best condition. Thank you for reading my wordy letters and drafts. Thank you for your strategic thinking, navigating me through the whole project as a voice of reason counselor and, of course, for your endless kindness, patience, and willingness to help.

I much appreciate the help from my co-supervisors, Professor Roger Chung, and Dr. Annemarie Nadort. They helped me to improve my writing and encourage me throughout the time we spend together. Moreover, thanks for all the constructive advice you gave about the preparation of the thesis.

I appreciate co-supervisor, Dr.Wei Deng. I may not have this opportunity to study at Macquarie University, if not for your help and encouragement during the scholarship application period.

A special thanks to Prof. Judith Dawes for help me review part of the literature review and gave some constructive feedback.

I am thankful to Professor Min Li. She encouraged me to pursue my dream and fight my way to it. She is not only my previous supervisor at Fujian Normal University but also my mentor and my role model. She leads me into the research area, and help me navigate my

way to where I am now. She does not only taught me how to learn knowledge and sharpen my skill but also taught me how to be a decent man.

A special thanks to Dr. Anna Guller. Thank you for helping me since the day we met and stayed by my side when I was almost going to quit. Thank you for all the useful tools and advice you shared with me. Thank you for sharing your life story, which inspired me a lot. This thesis will not be possible if you do not tell me not to give up. That conversion we had in August 2018 is crucial for me. You talked me out of the idea of giving up this study. You really like another mom to me. I simply can not thank you anymore.

My extraordinary and soulful gratitude goes to my collaborators involved in this project and our works in the field of hyperspectral imaging, who became my dearest friends and vice versa. Several notable names will be kept in my grateful heart forever for being my steadfast shoulders and a reliable team during these challenging times: Kashif Islam and Saabah Mahbub, thanks for all the discussion we had in the past few years, and all the problems you have solved for me. Thank you for your kindness and your patients. I am fortunate to have the chance to work with you guys. And also a big thanks to all my colleagues Aziz ul Rehman, Abbas Habibalahi, and Martin Gosnell.

I am grateful to Vlada Rozova, Peter Petocz, Ruth Oliver, Yan Wang, Shicheng Zhang, and Simone De Camillis. Thank you for your help in image processing, data processing, statistic, and MATLAB coding. Thank you for your time explaining all the things in detail to me. Thank Yan for formatting and providing this thesis templet.

Thanks, Ayad Anwer and Sinduja Subramanian, for performing all monocytes isolation, purification, characterization, and imaging procedures.

This work can not be done without the people who always helped me to stay active and motivated, shared their thoughts, and accepted myself in any state of mind ad mood. Thank you so much, dear Yan Wang, Yuan Liu, Sandhya Clement, Lianmei Liang, Sameera Iqbal, Kashif Islam, and Saabah Mahbub. I am also grateful to all the members of Ewa's group and those who helped in the CNBP: Wenjie Chen, Fei Deng, Fei Wang, Fang Gao, Zahra Khabir, Wan Aizuddin, Guozhen Liu, Jared Campbell, Chongfeng Guo, Yueyin Cao, Liuen Liang Xiaoxue Xu, Kai Zhang, Ke Ma, Yue Zhao, Hangrui Liu, Yue Cong, Laya Jose for their interest in the subject, understanding and support during my M.Phil study.

I am also thankful for the inspiring stories that carried me through my darkest time. I am grateful for Meiyun Lai, Yu Qin, Li Bian, Shiyin Xu, Hui Lin, Shen Jiang, Yao Wu, and Li Chen. Your stories encouraged me to fight until the end.

I also want to express my gratitude to our faculty staff members, who helped me in various practical aspects of the M.Phil life: Alex Fuerbach, Tracy Rushmer Jane Yang, Gina Dunford, Liz Bignucolo, Lisa Pesavento, Vivienne Wong, Danny Cochran, Emma Hastings, Ben Norton, Kelly Sharpless, Leonie Mckay, Jenny Morcom, and Amit Shrestha.

I want to express my gratitude to Shiguang Zhao from Anhui Polytechnic University, who was my first supervisor in science and taught me an uncompromising attitude to science.

I am grateful to Macquarie University for awarding me the International Macquarie University Research Excellence Scholarship (iMQRES). I want to thank ARC Centre for Nanoscale Biophotonics (CNBP) for financial support of the experimental expenses and the provided possibility to attend the national and international conferences during this project. Special thanks to the staff of the Department of Physics and Astronomy (Faculty of Science and Engineering), where my work and myself personally always can find reliable and professional help.

Many friends never gave up on me during all these years; they gave me strength and courage to march to the end. I am endlessly thankful to, Songqiu Zhou, Xiang Pin, Shanshan Shi, Li Kan, Kefan Chen, Wei Song, Kim Chao-Vo, Carmen Germain, Jingsi Jiang, Cuiting Chen, Wen Xu, Xi Zhao, Zibin Chen, Xin Xu, Yue Yu, Jiayuan Xie, Yue Du, Yonghe Han, Yi Zhong, Yina Huang, Mengxin Jiang, Tao Jiang, Hao Jiang, Hong Li, Liangyuan Li, Fan Yong, Kun Lin, Jing Liu, Yang Zhang, Weiyi Xue, Yun Zhou, Shuqi Qin, Zhen Song, Xin Su, Kai Sun, Yulong Sun, Yuan Tao, Yamu Tian, Haiqiao Wang, Ning Wang, Yue Wang, Zuozhen Wang, Chao Gao, Juan Han, Xing Xu, Yanli Xu, Li Yang, Da Yang, Wenxian Zhang, Yahong Zhang, Linjun Qi, Yameng Zheng, Tianfei Zhong, and Xiufang Sun.

Furthermore, a special thanks to some life-long friends who have been supported me for nearly three decades; you guys are always there to support me wherever I went and whatever I do. Thanks for always be on my side and help me overcome all the obstacles. I am glad that I can share all the joy, happiness, sadness, and everything with you. Thank you: Yongin Zhou, Yue Gu, Qian Feng, Yujia Hu, Yan Pan, Qiufeng Wang, and Zichuan Mao.

Finally, my incredible, caring, understanding, supporting, and unconditionally loving family. I can not survive without you, definitely. Furthermore, this is you who make this year-long science journey possible. Thank you for my mother, Jiangju Jiang, and Father Chunlin He brings me to this world. Thank you for raising me in a safe and happy environment, and thank you for allowing me to live my dreams. You let me know that there will always be someone that I can turn to. Thank you for tolerant my temper and help me to live a healthy life. And also, thanks for step-father Xiaoyong Huang. Thank you for taking care of my mother, and support me financially in the past few years, what you did for me and my mother allows me to fully committed in this study in the past few years. Thank you.

Thanks again for everyone who has supported and helped me, I will stay active and move to the next stage of life.

Statement of Contribution

In this research, the isolation preparation of monocyte, and the HSI imaging of monocyte were performed by Dr. Ayad Anwer and Dr. Sinduja Subramanian at the Department of Clinical Medicine Faculty of Medicine and Health Science, Macquarie University)

The imaging pre-processing, image processing, feature extraction, and statistic analysis were performed by myself.

Abstract

Extracting biochemical information from cell and tissue autofluorescence without using any external biomarkers is a promising approach for disease diagnosis and treatment. This thesis reports the advancement of fluorescence microscopy and image acquisition tools to observe autofluorescence signals, and I intended to use these signals as a biomarker for disease diagnosis and classification. In this research, I applied the hyperspectral imaging technique in observing the autofluorescence signals in peripheral blood monocytes from both healthy control and motor neuron disease patients. Current motor neuron disease diagnosis and classification methods are mainly based on clinical observations, which depends upon an experienced neurologist to make an informed clinical judgment. The development of an early-stage biomarker would be beneficial for the diagnosis of this disease.

Research presented in this thesis centers around the identification of distinct autofluorescence features from the peripheral blood monocytes, which can help reveal the difference between a healthy person and a motor neuron disease patient. From my result, a novel biomarker is discovered by applying the hyperspectral image technique. It is based on the mean cell intensity per unit area on a selection of channels. According to 15 samples, the classification methods showed promising results. With further validation, it may be applied in motor neuron disease classification.

Keywords: Hyperspectral imaging, Motor neuron disease, Autofluorescence, Monocyte, Biomarker, Classification

Content

List of Acronyms

AF	Autofluorescence
ALS	Amyotrophic lateral sclerosis
ANOVA	Analysis of variance
ATP	Adenosine triphosphate
BO	Bias Offset
BSA	Bovine serum albumin
CCD	Charge-coupled device
CMAP	Compound motor action potential
CMOS	Complementary metal-oxide-semiconductor
CNS	Central nervous system
CSF	Cerebrospinal fluid
DIC	Differential interference contrast
DNA	Deoxyribonucleic acid
DTI	Diffusion Tensor Imaging
EDTA	Ethylenediaminetetraacetic acid
EEG	Electroencephalogram
ELISA	Enzyme-linked immunosorbent assay
EM	Electron-Multiplying
EMCCD	Electron Multiplying CCD

FAD	Flavin adenine dinucleotide
FDA	U.S. Food and Drug Administration
FDG-PEG	Fluorodeoxyglucose positron emission tomography
FITC	Fluorescein isothiocyanate
FLAIR	Fluid attenuated inversion recovery
FMN	Flavin mononucleotide
FMN	Flavin Mononucleotide
FRET	Fluorescence resonance energy transfer
FWHM	Full width half maximum
GFP	Green fluorescent protein
GUI	Graph-user interface
HBS	Hanks balanced solution
HIS	Hyperspectral imaging
HS	Hyperspectral
IC	Internal conversion
ICCD	Intensified charge-coupled device
ISC	Intersystem crossing
LED	Light-Emitting Diode
LMN	Lower motor neurons
MND	Motor neuron disease
MRI	Magnetic resonance imaging

MSI	Multispectral imaging
MUNE	Motor unit number estimation and motor unit number index
NADH	Nicotinamide adenine dinucleotide
NADPH	Nicotinamide adenine dinucleotide phosphate
NASA	The National Aeronautics and Space Administration
NI	The Neurophysiological Index
NIR	Near-infrared
PBMC	Peripheral blood mononuclear cell
PBS	Phosphate-buffered saline
PET	Positron emission tomography
PMT	Photomultiplier
pNf-H	Phosphorylated neurofilament heavy subunit
PPS	Photons per pixel per second
PRNU	Photo-response nonuniformity
QE	Quantum efficiency
RGB	Red, Green, and Blue
ROI	Region of interest
ROS	Reactive Oxygen Species
SBM	Surface-based morphometry
SD	Standard deviation
SNR	Signal-to-noise ratio

TDP-43	TAR DNA-binding protein 43
TSPO	The translocator protein
TTL	Transistor-transistor-logic
UMN	Upper motor neurons
USI	Ultra-spectral imaging
UV	Ultraviolet
VBM	Voxel-based morphometry
vis	Visible

In Alphabetic Order

Chapter 1: Introduction

1.1 Introduction

Advances in fluorescence microscopy techniques have facilitated progress in the life sciences by developing new ways to observe complex biological processes, visualizing cellular structures and helping to uncover the functions of different parts of the cell [1, 2]. Usually, various types of targeted labeling with extraneous fluorophores have been used to reveal vital biochemical information from fluorescent microscopy images. Multiple fluorescent probes are required to relate various aspects of cellular processes to one another, and this is difficult both practically and at the level of data analysis, due to the potential for signal crossover and spectral overlap between different fluorophores` emissions. [3]

However, the large size of these fluorescent probes and the requirement that they need to be fused to functional proteins for detection means they can potentially affect normal cellular behavior leading to inaccurate observations. Autofluorescence, the fluorescence emitted by endogenous fluorophores, has come into the spotlight as a non-invasive way for investigating cell metabolism[4-6]. These endogenous fluorophores all have essential roles in cellular metabolism and can, therefore, provide autofluorescent signatures to monitor vital biological processes [7, 8]. Hyperspectral imaging has emerged as a novel method for cell classification. This technique can be applied for cellular characterization in health, disease, and during treatment since cells within changing physiological conditions display different metabolism states. Accordingly, hyperspectral signatures can be used as a biomarker for disease classification and continuous monitoring.

1.2 Statement of the problem

Motor neuron disease (MND) is an idiopathic, late-onset, and fatal neurodegenerative disease that is characterized by the progressive loss of motor neurons in the brain and spinal cord [9, 10]. The most common form of MND is called amyotrophic lateral sclerosis (ALS), which involves the progressive loss of function of both upper (UMN) and lower (LMN)

motor neurons. Importantly there are other forms of MND, or non-lethal mimic diseases, that affect either upper or lower motor neurons and display lower severity of symptoms. [10] Current MND diagnosis and classification methods are mainly based on clinical observations[11], reliant upon an experienced neurologist to make an informed clinical judgment. Importantly, there has been a significant advance in the understanding of the genetic origins of MND, with many disease-associated genes discovered [12-20]. This has allowed the proposal of many hypotheses and mechanisms to explain the underlying molecular cause of MND [10, 21-33]. These findings, in turn, has identified prospective biomarkers, which may support the potential classification and diagnosis of specific forms of MND or severity [34]. The lack of unbiased, quantitative tools for consistent and accurate diagnosis, and classification of the disease make a discussion on a patient's condition, and research communication more difficult. It is, therefore, critical to find a validated biomarker for diagnosis, classification, and therapy progress monitoring [35]. An accurate biomarker of disease progression is essential for evaluating the efficacy of new drug development [36] and would shorten the current diagnosis time for ALS patients (usually around one year from the onset of symptoms). [9]

1.3 Significance and novelty of this work

The primary purpose of this work is to develop a classification method to distinguish pre-symptomatic motor neuron disease patients from healthy individuals by observing metabolism changes in their isolated monocytes using hyperspectral imaging techniques. Hyperspectral imaging provides new windows into the biological functions of individual living cells and may be used to detect and quantify aspects of their metabolic activity. If successful, the capacity of hyperspectral imaging for high throughput and automation may provide a new diagnostic tool for clinical use.

1.4 Structure of the thesis

This thesis comprises five chapters. Chapter 1 contains the general introduction of the study of hyperspectral imaging technique and motor neuron disease (MND).

Chapter 2 outlines the important concept of hyperspectral imaging (HSI) and motor neuron disease. It discusses the potential for HSI to be used as a classification method for MND.

Chapter 3 presents an outline of the hyperspectral system used and gives a full description of the imaging protocols. It also includes the information for data analysis of hyperspectral imaging.

Chapter 4 presents the result for a potential classification method using the information extracted from a chosen set of channels from our HSI system. My approach has a 86% accuracy on our samples, but further validation is required on a more extensive data set.

Chapter 5 summarizes the whole work and discusses future works.

Chapter 2: Literature review

2.1 Hyperspectral Imaging

Hyperspectral imaging (HSI), which is also known as spectral imaging or imaging spectroscopy, is a method that integrates conventional imaging and spectroscopy, which allows us to gain both spatial and spectral information from a specimen [37]. The concept of "spectral imaging" was initially used for the area of remote sensing of the Earth; it was first defined by Goetz in the late 1980s [38-40]. Spectral imaging techniques include multispectral imaging (MSI), hyperspectral imaging (HSI), and ultra-spectral imaging (USI). These techniques are divided according to their spectral resolution, number of bands (each band represents a specific excitation and emission wavelength), width, and contiguousness of bands. [40] Since USI is not widely used in biomedical imaging, we will only compare HSI and MSI in this chapter when referring to spectral imaging.

HSI has been applied to many fields, such as pharmaceutical research [41-44], pharmaceutical production [45, 46], food sciences [47-56], food quality assurance [47, 48, 50-53, 55-57], forensic sciences [58-61], biochemistry and biomedicine [62-67], or cultural heritage [67, 68]. It has become an influential part of biomedical imaging, both in laboratory research and clinical diagnosis. It is reported that HSI is a potentially useful tool in measuring central changes of peripheral neuropathic injury and other neurodegenerative disease models. [69]

Our HSI system uses fluorescence microscopy along with an Electron Multiplying CCD (EMCCD) for data acquisition. Quantitative imaging methods will then be applied for data analysis. Details about HSI and our system setup will be discussed in Chapter 3

In this section, I will discuss the basic principle of fluorescence signal generation and detection, and the features of endogenous fluorophores. Then I will concentrate on explaining the basic concept for fluorescence microscopy and how quantitative imaging helps with data processing. Finally, I will demonstrate how our HSI system works.

2.1.1 Fluorescence and autofluorescence

Fluorophores are fluorescent chemical compounds which have the property that they absorb photons at a specific wavelength and emit photons at a longer wavelength. It means that the color of the emitted light is red-shifted when compared to the absorbed light. [70] The emitted light is usually known as fluorescence.

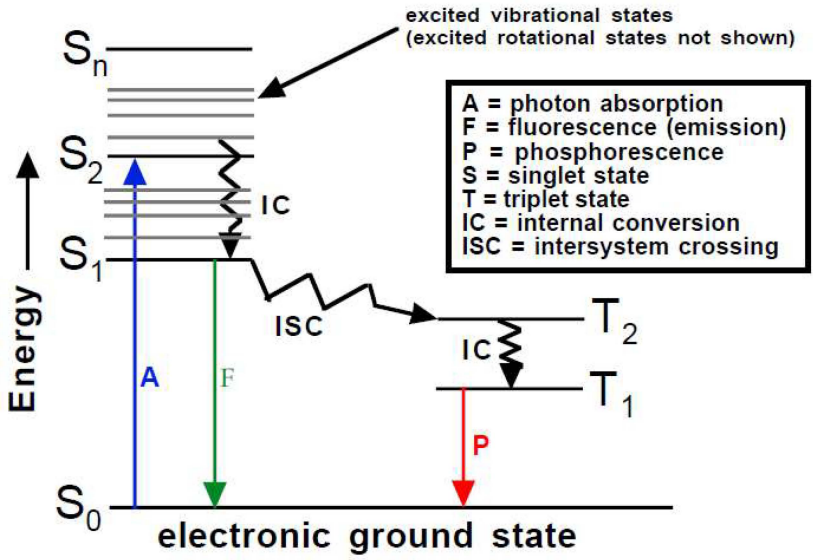

Figure 2-1 Absorption and emission of light depicted on a Perrin-Jablonski Diagram Images are taken from [70]

To understand how a photon can be re-emitted from fluorophores, we need to understand the different energy states of the molecule and how they interact with photons. The negatively charged electrons create chemical bonds between the positively charged atomic nuclei. Most stable molecules have an even number of electrons, and these electrons stay in different energy levels (i.e., orbitals). The electrons in the same energy states usually have opposite spin (spin is an aspect of the angular momenta in quantum physics used to describe the state of an elementary particle, which is carried within the particle itself [2]), All states with zero total electron spin are called singlet states, and given the label, "S". The electronic ground state is commonly a singlet state, designated as S_0. Upon absorption of light, one of the electrons jumps into another orbital, usually into the first excited singlet state, S_1. The spin of this excited electron, which was lifted from the ground state to an excited state, is often not flipped. The spin of the excited electron and the spin of the single electron which

was left on the original ground state are still antiparallel. The electron distribution in the molecule is altered after the energy from the photon has been absorbed.

However, the excited state of a molecule is unstable, since this redistribution of electrons weakens the bonds in the molecule. This excited electron can lose its energy via several mechanisms, for example, collisions with other molecules, reaction with other species, or by nonradiative deactivation processes, for example, internal conversion (IC), intersystem crossing (ISC) and vibrational relaxation [2]. The excited molecule may also emit a photon to return to a lower, relaxed state, though it may not be the same state as it originated in. The energy of the emitted photon will be equal to the energy difference between the initial and final state of the molecule. This emission of a photon is termed as fluorescence [2]. In some cases, the spin of the excited electron is flipped, and the total spin of the molecule is no longer zero, a triplet state is formed, designated as T_1. "Phosphorescence" is usually defined as the emission from T_1 to S_0. A summary of the excitation and various decay pathways is generally given in the form of a so-called Jablonski diagram (**Figure 2-1**), as shown below.

Although fluorescence is sometimes considered similar to phosphorescence, the most significant difference lies in how the electronic energy transition changes the electron spin. No changes in electron spin are involved in fluorescence. This process usually leads to a short-lived electron state. The excited state has a lifetime of less than 1×10^{-5} s. Electron spin usually changes during the process of phosphorescence. Compared to fluorescence, phosphorescence has a longer lifetime of the excited state - from seconds to minutes. The emission wavelength is longer than the excitation wavelength in both fluorescence and phosphorescence.

As described before, the essential property of fluorophores (or fluorochromes) is that they can re-emit light upon absorption of light. Many fluorophores are organic molecules with conjugated double bond systems. For example, molecules contain several combined aromatic groups or planar or cyclic molecules with several π bonds [2, 71]. These π bonds are usually weaker than other bonds, which means they are more likely to be excited upon absorption.

Fluorophores are divided into several categories based on their molecular complexity and synthetic methods, which are biomacromolecules, small organic molecules, synthetic oligomers and polymers, and multi-component systems [72].

In biology studies, the fluorophores may be naturally occurring molecules such as the amino acid tryptophan, ATP (adenosine triphosphate), porphyrins, and other cofactors. They can also be synthetic chemical fluorophores, such as fluorescein, rhodamine, ethidium bromide. Furthermore, they can also be genetically modified protein, like GFP (Green fluorescent protein). The fluorophores that are discussed in this thesis are natural organic biomolecules, such as NADH (Nicotinamide adenine dinucleotide), FAD (flavin adenine dinucleotide), and FMN (Flavin Mononucleotide) [2].

Many parameters are used to describe fluorophores. The first important parameter for fluorophores is the wavelength characteristics, such as excitation and emission wavelength. They are usually reported by three different spectra: absorption spectra, emission spectra, and excitation spectra. The Stokes shift is defined as the difference between maximum excitation and emission wavelengths. [73] The second parameter is the Molar absorption coefficient (in $Mole^{-1}cm^{-1}$), which is used to link the quantity of absorbed light, at a particular wavelength, to the concentration of fluorophore in solution. The third one is the quantum yield, which defines the efficiency of the energy transferred from incident light to emitted fluorescence. It represents the fraction of excited molecules which emit fluorescent photons. Another parameter is the fluorophore's lifetime (measured in picoseconds), which indicates the duration of a fluorophore's excited state before returning to its ground state. [74]

However, fluorophores are quite sensitive to the local environment; some of the emission parameters can vary due to changes in temperature and other factors. Besides, many different pathways can lead to non-radiative dissipation of the excited state energy, such as quenching, photobleaching, fluorescence resonance energy transfer (FRET), and solvent relaxation. Thus, we need to measure fluorescence in a controlled environment.

Autofluorescence (AF), also known as native fluorescence, is widely found in all kinds of organisms, because of the universal presence of endogenous fluorophores. Autofluorescence describes the fluorescence emitted by endogenous fluorophores within the biological samples themselves, rather than the fluorescence emitted from external fluorophores, such as artificial fluorescent dyes or genetically-modified fluorophores [6].

With the development of microscopy and spectrofluorometry technology in the 20th century, autofluorescence was first reported by Stübel, a physiologist at Jena University, in 1911 [5]. It soon led to the synthesis or modification of highly selective and sensitive

fluorescent dyes for cell labeling. Autofluorescence is often considered as noise in exogenous and induced fluorescence-based assays, and they need to be optical filtered or bleached.

However, one disadvantage of exogenous fluorescent dyes is that they may interact with cells and interfere with the observation of normal cell activities. Meanwhile, endogenous fluorophores do not introduce such problems. Moreover, the autofluorescence emission is a direct reflection of the cell's biological substrate condition, since most endogenous fluorophores are commonly involved in cellular metabolism, cellular signaling, and other biological activities [5] It is an outstandingly powerful resource for the direct monitoring of cell activities. It is reported that endogenous fluorophores in plants have more favorable spectral properties and quantum efficiency than that in animals, thus they can provide a more detectable signal for morphology and physiology analysis. [5]. Several articles and books reviewed the application of autofluorescence in optical biopsy for obtaining diagnostic information as a minimally invasive method [4-6, 75-84]. Observing autofluorescence has become an extraordinary method to reveal diagnostic information *in situ* without introducing exogenous markers. Since the amount and distribution of endogenous fluorophores are easily affected by the morphological and metabolic conditions of biological samples, it makes endogenous fluorophores an ideal intrinsic biomarker for measuring the changes in the microenvironments of cell or tissue.

It is reported that many endogenous fluorophores can reveal the states of certain biological activities, [5] for example, NAD(P)H, flavins indicate the states of energetic metabolism; lipofuscins and lipofuscin-like fluorophores act as biomarkers in aging, oxidative damage, and more; porphyrins indicate alteration of heme metabolism. These endogenous fluorophores can help us distinguish cells that are in different pathological states, and are listed in **Table 2-1** [4, 78].

Table 2-1 Recent reported Endogenous fluorophores

Endogenous fluorophores	**Biological constituents**	**Autofluorescence (ex) / (em) ranges**	**Autofluorescence photophysical fingerprints and possible correlated alterations**
Aromatic amino acids: Phe, Tyr, Trp	Functional proteins	(240-280 nm) / (280-350 nm)	Spectral shape and amplitude (near UV, blue region tail)

Cytokeratins	Intracellular fibrous proteins	(280-325 nm) / (495-525 nm)	Spectral shape and emission amplitude
Collagen/Elastin	Extracellular fibrous proteins	(330-340 nm) / (400-410 nm) (350-420 nm) / (420-510 nm)	Excitation light birifrangence effects spectral shape and emission amplitude, depending on maturation degree in eldering and fibrosis
NAD(P)H	Coenzymes of key enzymes in redox reactions	(330-380 nm) / (440, 462 nm, bound, free)	Spectral shape, emission amplitude (NAD(P)H bound/free, NAD(P)H total/oxidized
Flavins	Coenzymes of key enzymes in redox reactions	(350-370;440-450 nm) / (480/540 nm)	flavins ratios, depending on aerobic/anaerobic energetic metabolism, antioxidant defense, inflammation, carcinogenesis
Fatty acids	Accumulated lipids	(330-350 nm) / (470-480 nm)	Spectral shape, emission amplitude, and photosensitivity depending on altered lipid metabolism
Vitamin A	Retinols and carotenoids	(370-380 nm) / (490-510 nm)	Spectral shape, emission amplitude, and photosensitivity depending on multiple functions including antioxidant and vision roles, and altered retinol metabolism
Protoporphyrin IX and porphyrin derivatives	Protein prosthetic group	(405 nm) / (630-700 nm)	Spectral shape, emission amplitude, and photosensitivity depending on heme and iron altered metabolism
Lipofuscins/ Lipofuscin like-lipopigments/ceroids	Miscellaneous (proteins, lipids, retinoids)	(UV, 400-500 nm) / (480-700 nm)	Spectral shape, emission amplitude depending on eldering, oxidation degree, cell stemness degree

Since each endogenous fluorophore has its unique fluorescence profile (as shown in **Figure 2-2**), they can be distinguished and quantified by quantitative analysis. A rich information dataset from these endogenous fluorophores can provide us with more insight into the understanding of cells that are in different states or undergoing different biological processes [4, 5, 78, 80, 85]. It is reported that features like channel ratios could be used as an imaging biomarker for redox ratios, which could further reveal the state of metabolism that linked to certain diseases. [86-89].For example, the ratio for NADH/NADPH could be measured by HIS, which further indicates the changes in redox ratios. In some studies, it is used to indicates the states of breast cancers [88, 89].

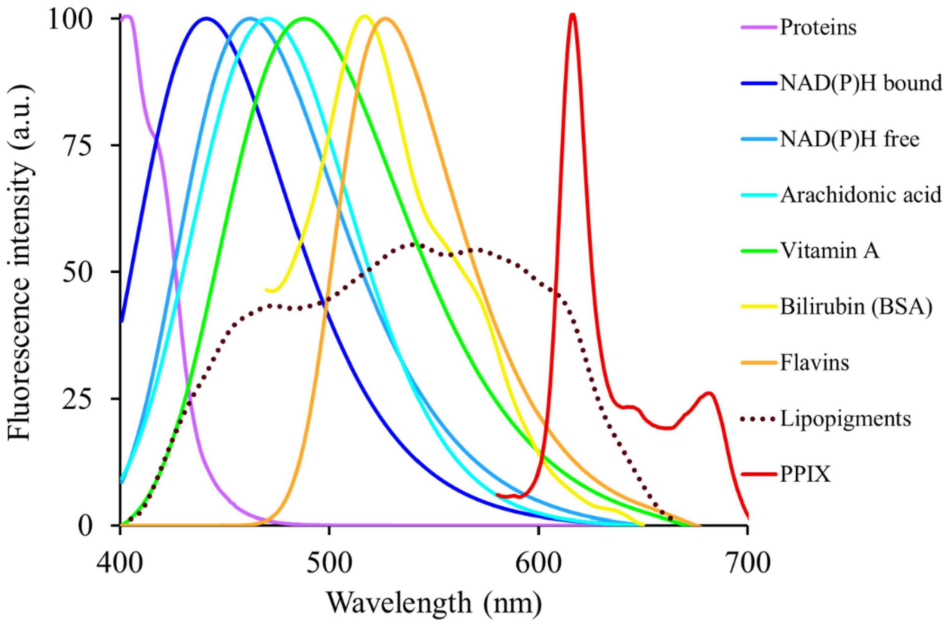

Figure 2-2 Typical spectral profiles of autofluorescence emission from single endogenous Fluorophores. Adapted from “. Autofluorescence spectroscopy and imaging: a tool for biomedical research and diagnosis” by Croce, A. C. and Bottiroli, G., 2014, Eur J Histochem, 58, 2461. Copyright 2014 by " A.C. Croce and G. Bottiroli." Adapted with permission.

To understand the information provided by these endogenous fluorophores, we need to have a deeper understanding of the data acquisition techniques and the data analyzing methods used in fluorescence microscopy and hyperspectral imaging. This is discussed in the following section.

2.1.2 Fluorescence microscopy

A typical fluorescence microscope is quite similar to a light microscope in overall design, except it is accompanied by a specialized excitation light source and filter set or filter cube.

Figure 2-3 shows a simplified schematic of an epi-illumination fluorescence microscope; it is a preferred design in modern fluorescence microscopy. Take the Stokes shift into consideration, and it is simple to imagine how to build a fluorescence microscope: illuminate the sample at a chosen wavelength and filter the emission light at a longer wavelength so that only the emission fluorescence can be seen [90]. In this section, we discuss each fundamental component in a fluorescence microscope.

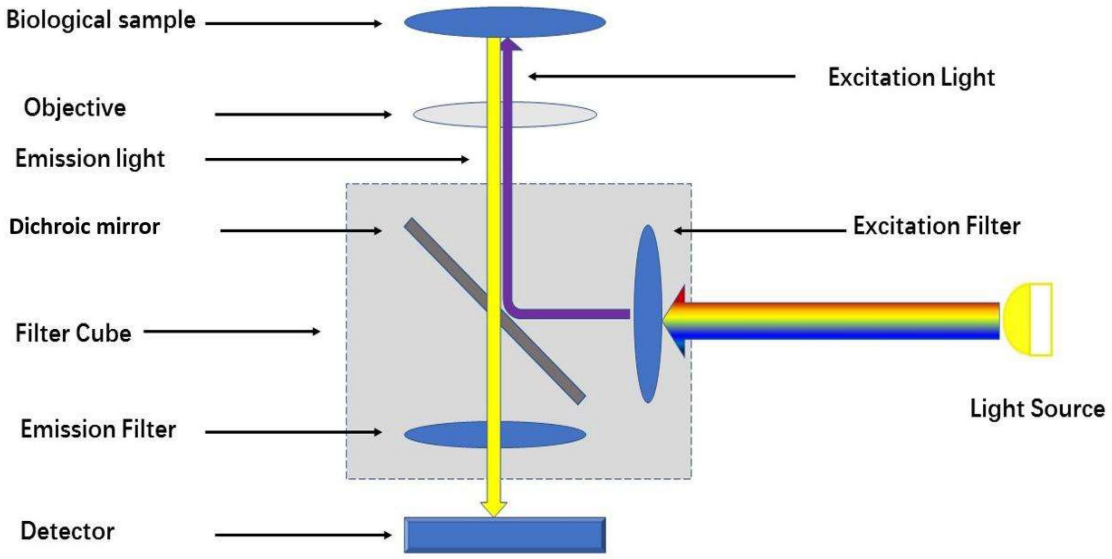

Figure 2-3 Simplified schematic diagram of a fluorescence microscope (epifluorescence)

A typical fluorescence microscope contains two sources of light. One is used for illuminating the biological sample in the transmitted mode for initial viewing; it is usually a halogen lamp. The other is the excitation source, usually mercury arc lamp, xenon arc lamp, laser, or LED (Light-Emitting Diode), which is used for exciting the specimen.

One essential requirement of a fluorescence microscope excitation light source is that its emission spectrum closely matches the excitation spectrum of the fluorophores so that an image with a high signal-to-noise ratio (SNR) can be captured. Wavelengths that match the fluorophore strengthen the signal, but any nearby wavelengths generate background noise that can outweigh the signal emitted by the object of interest. Mercury arc lamps and xenon arc lamps are very convenient sources of excitation since they have a broad spectrum, so they are suitable for several typical fluorophores. However, due to the instability and uneven illumination of these lamps, they are not suitable for quantitative analysis [70].

Meanwhile, the laser has become another light source for fluorescence microscopy. Lasers emit light at discrete wavelengths and are well known for high stability both spatially and temporally – both on a short and long timescale [70]. Laser light can be easily be focused on the specimen plan compared to the mercury arc lamp. However, their high cost, limited wavelengths, and potential risk have confined their use [91].

Furthermore, high brightness LEDs across the visible spectrum has emerged as a new light source. LEDs are semiconductors that exploit the phenomenon of electroluminescence, in which a material emits light in response to the passage of an electric current [92]. LEDs are available throughout the UV/Vis/NIR-spectrum with a narrow bandwidth. They are easy to maintain and have a long lifetime, besides, they can be switched in nanoseconds, and they do not require warm-up and cool down. These features make them ideal light sources for fluorescence microscopy [70, 92-94]. Moreover, the LED source can be easily connected to the microscope via a liquid light guide, and they can provide a more uniform excitation across the field of view [93].

In a fluorescence microscope, the light at specific wavelengths (related to particular fluorophores) needs to be selected and separated from others. One desirable way is by using filter cubes, which are small block-shaped filter holders composing of the excitation filter, dichroic mirror, and emission filter [90], By fitting filter cubes into a circular carousel or linear block that can hold several different cubes, it makes switching these filter cube easily and rapidly possible, either manually or automatically. [95]

Filters usually have different transmission properties. For example, a short-pass filter will only allow light shorter than a particular wavelength to pass, while a long-pass filter only allows light longer than a specific wavelength to pass through the filter. Besides, both wide band-pass and narrow band-pass filters exist based on the width of wavelength they allow to pass [96]. The narrower the range of wavelengths the filters are, the less the intensity is allowed to pass, which will result in a weaker signal [96]. However, this also means the system is more capable of discriminating individual fluorophores in a mixture (i.e., better contrast). Meanwhile, broadband filters provide more signal, but less contrast [95]. Other wavelength-selection devices, like monochromators and electro-optic instruments, are also widely used. Meanwhile, dichroic mirrors are another useful tool in filter cube manufacture, because they can reflect the shorter wavelengths excitation light and allow the long-wavelength emitted light to pass. It prevents the excitation light from either the detector so

that the image is corrupted by excitation light [95]. Given the Stoke shift, it is easy to choose the right filter cube for the fluorophores of interests.

In the early years of fluorescence microscopy, light-sensitive films were used for image recording, but with the development of electronic light detectors, it was possible to capture fluorescence images in a numerical, digital form. This advancement in image capturing methods, along with the development in image digitalization, analysis, and storage methods, have made a significant contribution to quantitative fluorescence microscopy.

A variety of detectors are used in modern fluorescence microscopes, such as the charged-coupled device (CCD), Electron Multiplying CCD (EMCCD) complementary metal-oxide-semiconductor (CMOS) active pixel detector, and photomultiplier tube (PMT). [70]

The most commonly used light detector in a standard widefield fluorescence microscope is a CCD camera. It offers excellent SNR and a relatively low price when comparing to EMCCD and CMOS detector. EMCCD provides high performance when imaging in low light level with speed, for example, single-molecule fluorescence. CMOS is useful for microscopy when speed is vital, combined with its high sensitivity and large field of view. Meanwhile, PMTs are used in applications without spatial resolution, such as laser scanning confocal microscopes. Other types of light detectors, such as intensified charge-coupled device (ICCD), and avalanche photodiodes (APDs), are becoming essential in modern fluorescence microscopy. [70]

Although fluorescence microscopy has opened a new window for the biologist, especially in live-cell imaging, its use is still limited by some significant issues. The first one is photobleaching. Fluorescent molecules can be photochemically destroyed when interacting with surrounding molecules; they permanently lose their ability to fluoresce. This phenomenon affects the collection of high-quality image data. The second issue is phototoxicity. Under high-intensity illumination, the excited fluorescent molecules are more likely to be involved in free radical production with molecular oxygen. These free radicals are highly active and unstable. They can damage subcellular components and compromise the entire cell. [97, 98] This process might interfere with the observation. The last issue is the limited spatial resolution of images. The optical resolution of fluorescence microscopy depends on the wavelength of the light that builds the image, and it is also impacted by the numerical aperture of the lens. This makes it impossible for fluorescence microscopy to distinguish features less than ~250 nm. In other words, any objects that are smaller than

~250nm can be misinterpreted from the fluorescence image. Besides, only a few fluorophores can be measured simultaneously in one specimen, because, currently, some have close wavelengths that cannot be distinguished due to the limitation of filter cube settings; some fluorophores with similar colors may appear in the same wavelength in the fluorescence image.

2.1.3 Hyperspectral imaging

Hyperspectral imaging (HSI) was first applied in remote sensing by NASA in the early 70s [39], It was then modified for application in several different fields including biomedical research, agriculture, food safety, and forensic sciences. [38-40, 57, 59, 61, 64, 65, 68]. It has shown great potential in distinguishing and quantifying different fluorophores. Only gray or RGB images from a biological specimen can be captured by traditional biomedical spatial imaging. Features extracted from these images are usually spatial properties such as shape, size, and texture. However, limited information can be provided by these features for early detection and identification of cell abnormalities [40].

The HSI used in biomedical research combines the strength of both fluorescence microscopy and spectrometers. It obtains not only a 2-D spatial image but also acquires spectral information from each pixel. Another spectral imaging method, multispectral imaging (MSI) is similar to HSI but has two main differences: 1) HSI usually acquires images from tens to hundreds of bands (or “channels”, each represent a specific excitation/emission wavelength) while MSI only captures a few bands; 2) HSI continuously measures the spectrum, while MSI usually measures selective, non-continuous bands [99]. HSI is more sensitive to complex spectral changes when comparing to MSI because it acquires more information spectrally. HSI exhibits extraordinary power in discriminating multiple chemical species, especially when their emission spectra are partially overlapped. [100]

In biomedical imaging, with the ongoing discovery of exogenous biosensors, such as fluorescent proteins [100], quantum dots [101], and organic fluorophores [102] and the revelation of various endogenous chromophores, such as NADH, FAD, and Tryptophan, these findings made the widespread application of HSI possible. In order to take advantage of these exogenous and endogenous fluorophores, imaging systems must have the ability to measure the spectroscopic variations of several fluorophores together. This requirement is because most cellular responses do not take place independently, and there is a combination

of fluorophores changes that occur in response to cellular events simultaneously. It requires the HSI system to have excellent resolution, both spatially and spectrally, to observe these events in vivo. [99]

One drawback of relying on conventional diagnostic imaging methods, which can be easily overcome by HSI, is that there is sometimes a lack of sufficient information. In most cases, even with the progress of the disease, however, there are no significant changes in the morphology or color characteristics in abnormal cells, which can lead to the delay of accurate diagnosis. Meanwhile, the information extracted from HSI can potentially provide crucial pieces of evidence for cellular metabolism changes due to diseases, since it can monitor fluorophores that are involved in cellular metabolism. One of the two main advantages of HSI is that it can image a combination of different fluorophores with a universal experimental setting without changing filter settings. Another advantage of HSI is that it improves the efficiency of the unsupervised linear spectral unmixing, which is an efficient information extraction method for HSI. It is one of two unmixing methods that can distinguish different components from a mixture without knowing which specific components are in the mixture [99]. Meanwhile, the other method, called supervised linear spectral unmixing, requires specific information to perform the unmixing procedure, including the exact number of fluorophores in the mixture and their emission spectra. However, if that information is either hard to acquire, as unknown chemicals are present in the mixture, e.g., for in vivo tissue measurements, or unreliable to use, as when the fluorophores' spectra are subject to change due to experimental and biological environment, the supervised spectral unmixing is most unlikely to succeed. In these situations, HSI's continuous spectral sampling becomes crucial because optimizing the wavelength of interested channels, as described earlier, is impracticable [99, 103].

The essential parts of an HSI system are similar to that of a standard microscope, which includes hardware, data acquisition software, and pre-processing software. It also requires appropriate image processing methods and data analysis methods to unlock the potential of an HSI system fully.

2.1.4 Image processing

After the hyperspectral image has been obtained, it is important to perform image pre-processing to generate an accurate image for further analysis. The first important step is illumination correction, to correct the inhomogeneous illumination caused by misaligned

optics, dust, nonuniform light sources, or vignetting [104, 105]. The consequence of ignoring illumination correction often leads to intensity loss in dim areas, which can be up to 50% in scientific complementary metal-oxide-semiconductor (sCMOS) cameras [105]. However, these issues are often underestimated by many researchers.

There are two kinds of illumination correction methods. One is called prospective methods, which use a set of reference images to help estimate the correct surface. It requires either a set of bright images or dark images or a combination of both bright images and dark images to help correct the sample images. However, when reference images are corrupted or unavailable, it would be impossible to use prospective methods. Retrospective methods would be more appropriate for this situation since they only rely on actual images. Retrospective methods estimate the illumination pattern based on several non-related actual images, then substrate this pattern to restore the images to its ground truth.

After the images have been corrected, it is also important to get rid of the noise from the images. The noise intrinsic in hyperspectral imaging and the restricted ability of hyperspectral imaging tools presents one of the greatest difficulties in image pre-processing. The objective of image pre-processing is to enhance the visibility of certain image characteristics for subsequent assessment or display of images. The pre-processing method does not improve the intrinsic content of data but merely emphasizes it [106].

The advances in digital imaging sensors in past decades have resulted in a wide range of use of digitally processed cameras[107]. Nevertheless, the SNR limits the extraction from the images of helpful data. Although image noise sources for CCD[107] are well documented, little research has been accomplished to evaluate and validate the EMCCD noise sources. In this chapter, the noise components are presented and discussed based on previous work [8, 108, 109].

According to previous research, imaging noises are divided into different types, including spatially fixed noise, temporally varying noise, and digital processing based noise. [110] The spatially fixed noise is known as illumination independent noise, which consists of reset noise, combined thermal noise, combined flicker noise, readout noise (N_{read}), dark current shot noise (N_{dc}), and offset fixed pattern noise (N_{offset}). On the other hand, photo-response nonuniformity ($PRNU$) and photon shot noise (SN_{ph}) are temporally varying noise [110]. This temporally varying noise is illumination dependent noise. Furthermore, digital processing-based noise consists of quantization noise (N_Q) and EM gain noise. The noise

model for the EMCCD camera was summarised from the previous study, and shown below[107, 108, 111]. **Table 2-2** shows the most common EMCCD noise. [8, 81, 107, 108, 111-116]

Table 2-2 Noise elements for EMCCD camera

Noise Type	Origin	Manifestation	Dependencies
Illumination-Independent Noise Types			
N_R, *reset noise.*	CCD support IC.	Additive temporal and spatial variance.	Temperature.
N_{therm} combined thermal noise.	CCD support IC's.	Additive temporal and spatial variance.	Temperature.
N_{other}, combined flicker noise, dark transistor currents, and other minor contributors.	CCD sensor and CCD support IC's.	Additive temporal and spatial variance.	Temperature, CCD readout rate.
N_{read}, readout noise. Combined $N_R+N_{therm}+N_{other}$.	As per N_R, N_{therm}, and N_{other}.	Additive temporal and spatial variance	Temperature, CCD readout rate.
N_{dark}, dark-current shot noise.	CCD sensor.	Additive temporal and spatial variance.	Temperature, exposure time.
FPN, offset fixed-pattern noise.	CCD sensor.	Additive spatial variance only.	Temperature, exposure time
Illumination-Dependent Noise Types			
PRNU, photo response non-uniformity.	CCD sensor.	Multiplicative spatial variance only.	Incident pixel illumination.
N_{shot}, photon shot noise.	CCD sensor.	Additive temporal and spatial variance.	Incident pixel illumination.
N_{CIC}	EM gain register.	Poisson noise component	Vertical shift speed, clock level, shape
F	EM gain register.	Uncertainty added to all input components	Hardware,

Digital Processing Noise Effects Types			
N_D, *demosaicing noise.*	CCD support IC.	Multiplicative noise amplification or attenuation.	Demosaicing implementation, combined sensor noise.
N_{filt}, post-image-capture effects.	CCD support IC.	Multiplicative noise effect.	Parameters for image enhancement, combined sensor noise.

The illumination-independent noises are mostly temperature related; they can be minimized by the CCD-sensor's cooling system [8, 117]. The illumination-dependent noises include pepper & salt noise, which is caused by cosmic ray and other abnormal activity from detector pixels, and the median filter can remove it. Furthermore, it can also be additive Gaussian distributed noise, which can be removed by spatial domain filters [110, 118, 119].

After the image pre-processing procedure, there are also a few optional steps that can be taken before data analysis, including image enhancement, image segmentation, and object measurement. Image enhancement is aiming at increasing the contrast between signal and noise/background; it will be helpful for future segmentation procedures, especially for automatic segmentation. The commonly used methods include histogram equalization[120], convolution and spatial filtering, Fourier transform and wavelet thresholding, etc [121, 122]. Then the images would be segmented based on the region of interest (ROI), in cell biology research, it is usually referred to the cell itself. Many algorithms have been developed to perform this procedure; they usually based on different features, such as contrast, local intensity changes, or textures. Some examples are the threshold, edge detection, and morphology operation, respectively [106].

Subsequently, it is also essential to extract the features from the images for data analysis. The widely used features are intensity features, texture features, and morphology features. After these features have been quantified, these data will be used for data analysis.

2.1.5 Data analysis

The data analysis methods for HSI usually serve one of the following purposes: classification and quantification. In the biomedical field, classification can help determine

cell type [7, 123], cellular metabolism states [124], disease diagnosis [125], and so on. Furthermore, quantification is usually used to determine one or more of the fluorophores inside specific cells and can also be used to monitor the changes within certain cellular activities. [24, 126, 127] The general workflow is to use classification methods to determine which group the sample belongs to, then use endmember extraction to determine the components of the sample, and finally, use unmixing methods to determine the relative quantity of each endmember within a sample [128].

2.2 Motor neuron disease

Motor neuron disease (MND) is an idiopathic, late-onset fatal neurodegenerative disease that is characterized by the progressive loss of motor neurons in the brain and spinal cord [9, 10]. MND has an average incidence of around 1 to 9 cases per 100,000 worldwide. Amyotrophic lateral sclerosis (ALS) is considered the most common subtype of MND, with around 80%–90% of MND cases diagnosed as ALS. [129] ALS is commonly referred to as motor neuron disease (MND) in the UK and as Lou Gehrig's disease in the USA [130]. The mean age of onset in individuals without a known family history is 56 years, which is around ten years later compared to those in individuals with familial ALS. The average life expectancy of MND patients in Australia is about 2.5 years from the time of the first onset, but it can vary significantly [131]. Even though significant advances in the genetic understanding of the disease [10, 22, 32, 129, 131, 132], the exact molecular mechanisms behind MND are still unclear. Riluzole is the only extensively used FDA-approved disease-modifying medicine for MND before 2017, can only prolong the life expectancy for MND patients for three months on average [133]. The newly approved medicine edaravone only works under strict inclusion criteria; its efficacy still needs to be further explored.

In this section, I am going to provide a brief introduction to MND, challenges in disease diagnosis, and the effect of the disease upon the immune system.

2.2.1 Challenges in MND diagnosis and classification

MND is considered a group of diseases that cause the selective degeneration of motor neurons in the brain and spinal cord [23]. As a consequence, this will then lead to muscle weakness and paralysis until the inevitable death caused by respiratory failure. [18, 134] However, it is now recognized that MND not only represents a group of different diseases,

but within each disease subtype, there is a spectrum of clinical complexity with regards to the age of onset, clinical manifestation, and severity. [134, 135] While these parameters can be determined from clinical evaluation, it can be a slow process and often only possible at later stages of the disease. Therefore, it would be valuable to develop a simple, unbiased, quantitative approach to improve patient classification.

Current MND diagnosis and classification methods are primarily based upon clinical observations. The most widely used test is called the El Escorial criteria [11] and its modified versions [18]. However, it is a subjective evaluation reliant upon an experienced neurologist to make the judgment on rating scores. Methods such as neuroimaging and have been introduced to aid the diagnosis progress, where they have proven valuable in excluding mimic diseases from misdiagnosis [136]. However, they are unable to distinguish different forms of MND, and they can not estimate the severity of the disease. **Table 2-3** gives a summary of variants and mimics of MND.

Table 2-3 Summary table of motor neuron disease and key features with each mimic/variant.

MND	Key feature	Differentiating/key category	Subtype category
ALS (Amyotrophic lateral sclerosis)	*Bilateral symmetric T2 and FLAIR hyperintensities anywhere along the corticospinal tract superiorly from the cortices extending caudally to the brain stem*	*Radiographic*	*Primary*
PLS (Primary lateral sclerosis)	*In contrast to ALS, PLS often involves the parietal and occipital lobes, while sparing the temporal lobes. On PET studies, PLS shows hypometabolism in the precentral cortex, while ALS can have frontal lobe involvement, which is not seen in PLS*	*Radiographic*	*Mimic*

SBMA (Spinal and bulbar muscular atrophy)	*Atrophy of the anterior and posterior horns of the spinal cord in addition to the facial, tongue, and respiratory muscles. Involvement of the muscles of mastication is characteristic*	*Radiographic*	*Mimic*
PPS (Postpolio Syndrome)	*Symmetric T2 hyperintensities within the substantia nigra, pons, medulla, anterior horns of the spinal cord, and ventral nerve roots. In addition to the CNS findings, MRI can also show T1 and T2 hyperintensities within the gluteal musculature without inflammatory changes*	*Radiographic*	*Mimic*
PBP (Progressive bulbar palsy)	*T2 hyperintense bands in the frontal lobe, corona radiata, internal capsule, pyramidal tract, and the brainstem*	*Radiographic*	*Variant*

MRI: Magnetic resonance imaging, CNS: Central nervous system, FLAIR: Fluid-attenuated inversion recovery, PET: Positron emission tomography

2.2.2 MND biomarkers

It remains a significant challenge to identify a minimally-invasive biomarker of disease onset or progression. Several potential biomarkers have been reported in recent years. Some showing promise for disease classification and diagnosis [34]. Table 2-4 shows a summary of these biomarkers.

Table 2-4 Diagnosis and classification biomarker for ALS [30, 34-36, 137-142]

Biomarker Type	Testing subjects	Measurement methods	Examples	Reference
Protein-based marker	CSF, blood	ELISA, Mass, spectrometer, western blot, etc.	$p75^{ECD}$,TDP-43, Ratio of CD14 to S100β, pNfH, MCP-1, etc.	[137, 140, 143-146]
Genomic biomarkers	Somatic cell	DNA sequencing	SOD1, TARDBP, FUS, etc.	[147-149]
Biological fluid-based biomarker	Blood, Urine	Blood test	Uric acid	[150]
Neuroimaging Biomarkers	Brain and spinal cord	MRI, PET,	VBM, SBM, FDG-PEG, TSPO-PET, etc.	[151-156]
Electrophysiological Biomarkers	Nervous system	Nerve conduction studies and needle electromyography.	CMAP, NI, MUNE, etc.	[157-159]
Another test	Skin, urine	Skin biopsies, Urine analysis.	Bedsores, $p75^{ECD}$	[160, 161]

CSF: Cerebrospinal fluid, ELISA: Enzyme-linked immunosorbent assay, p75ECD: extracellular domain of p75. pNf-H: Phosphorylated neurofilament heavy subunit, VBM: Voxel-based morphometry, SBM: Surface-based morphometry DTI: Diffusion Tensor Imaging, TSPO-PET: The translocator protein, FDG-PEG: Fluorodeoxyglucose positron emission tomography, CMAP: Compound motor action potential, NI: The Neurophysiological Index, MUNE: Motor unit number estimation and motor unit number index

Since MND is a complex disease, it is highly likely that multiple pathogenic processes are involved during the progress of the disease. This includes neuronal dysfunction, the accumulation of insoluble proteins, and neuroinflammation. These abnormalities may eventually be reflected by detectable changes in blood or CSF. However, because of disease complexity, a panel of biomarkers may likely be more informative. Alternatively, another solution may be to develop a method that can monitor the dynamic change of several biological processes simultaneously [36].

2.2.3 Hypothesis about MND mechanism

In the past three decades, several hypotheses have been proposed, including excitotoxicity, structural and functional abnormalities of mitochondrial, impaired axonal structure and transport defects, altered energy metabolism free radical-mediated oxidative stress, and neuron inflammation, [22, 27, 30, 31, 33, 132, 162, 163]

Excitotoxicity is caused by over-stimulation of receptors for excitatory amino acids (such as glutamate), resulting in neuronal death mediated by cellular calcium influx [164, 165]. For example, abnormal levels of the astrocytic glutamate transporter EAAT2 have been reported in a study of human post mortem brain and spinal cord tissue [166]. Moreover, experiments in SOD1 transgenic mice have shown that overexpression of EAAT2 can delay the progress of motor neuron degeneration. [167, 168] Although the exact mechanism remains unclear, it is worth noting that riluzole, an FDA-approved treatment for MND, seems to have anti-glutamatergic activity [169].

Mitochondrial dysfunction is widely observed in tissues that are affected by MND, especially for patients with mutant SOD1. Mitochondria serve as a powerhouse for the cell, which is critical for the survival of the cell [30]. It is reported that mutant TDP-43 and mutant SOD1 can affect the expression of proteins involved in energy metabolism in mitochondria [17, 19, 148]. However, whether mitochondrial dysfunction is the cause or result of neurodegeneration is still unclear. [170, 171]

Altered energy metabolism states have been clearly illustrated in animal models, showing that whole-body energy physiology is effected in MND due to neurodegeneration. [172, 173] These metabolic changes can be observed within circulating blood and can be correlated with survival or functional status [174-176]. It has therefore been reported that measures of altered metabolism can be used as a biomarker for disrupted mitochondria. [177]

Oxidative stress is caused by excessive production of Reactive Oxygen Species (ROS), the side products of healthy cellular metabolism (See **Figure 2-4**) [178]. Most ROS are oxygen free radicals, and they are involved in oxidative damage [179]. Under normal circumstances, these ROS are consumed by endogenous antioxidants, and the rate of generation for antioxidants is similar to that of ROS. However, once this balance is broken, oxidative damage can quickly affect normal cell function and health. Studies from post-mortem tissue analysis have observed oxidative damage to proteins, lipids, membranes, and DNA as consistent pathological disease features. [180] Furthermore, mutations in the SOD1 gene (which produces a critical antioxidant protein) are responsible for 20% of familial MND. [181, 182]

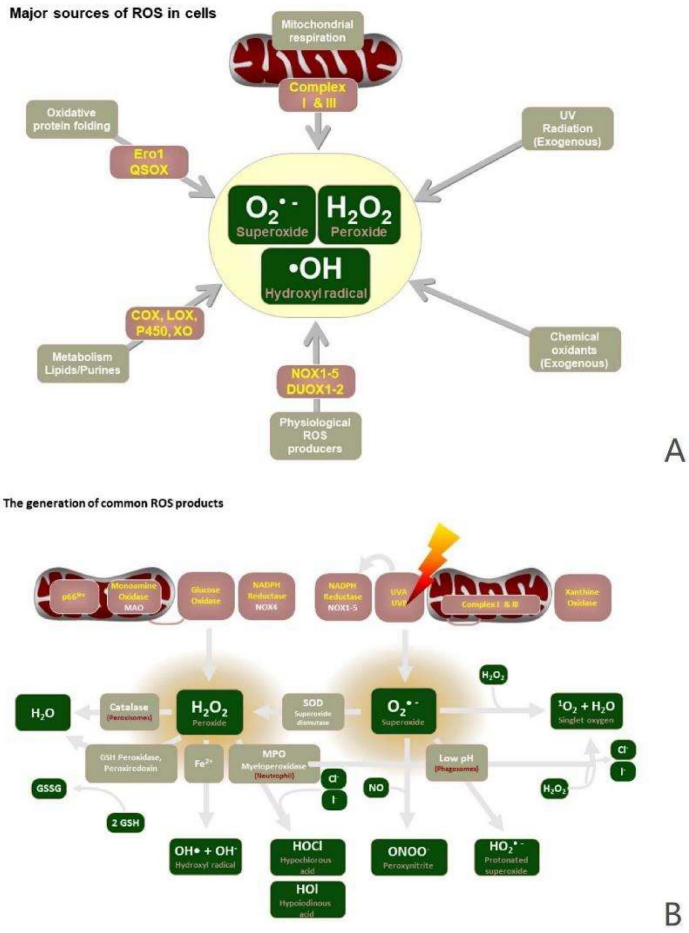

Figure 2-4 ROS in the cell. A.) Significant sources of ROS, B.) Generation of conventional ROS products [21, 181-185].

Another potential influence upon disease pathogenesis is neuroinflammation, which is supported by the evidence of activation and proliferation of microglia (the resident immune cell in the CNS) in the areas of the CNS affected by MND [22, 185]. Microglia usually exist in a relaxed state in the healthy brain, with a small cell body and minimal expression of surface antigens [22]. Once they are activated due to injury or neurodegeneration, they will release several factors into the CNS, such as glutamate, ROS, proinflammatory cytokines, etc. in order to kill pathogens or remove debris [185, 186]. However, these factors may act on neuron directly to induce cell death, [186] The release of these inflammatory molecules from active microglia may affect astrocytes, and result in increased release of neuroinflammatory mediators which will result in more activated microglia. This creates a potentially lethal cycle [187]. Although neuroinflammation may have a strong influence on

neurodegeneration, there is evidence that there might be a cross-talk between neuroinflammation and oxidative stress, highlighting the complexity of disease mechanisms.

A summary of some of the proposed mechanisms and hypotheses discussed above are shown in **Figure 2-5**.

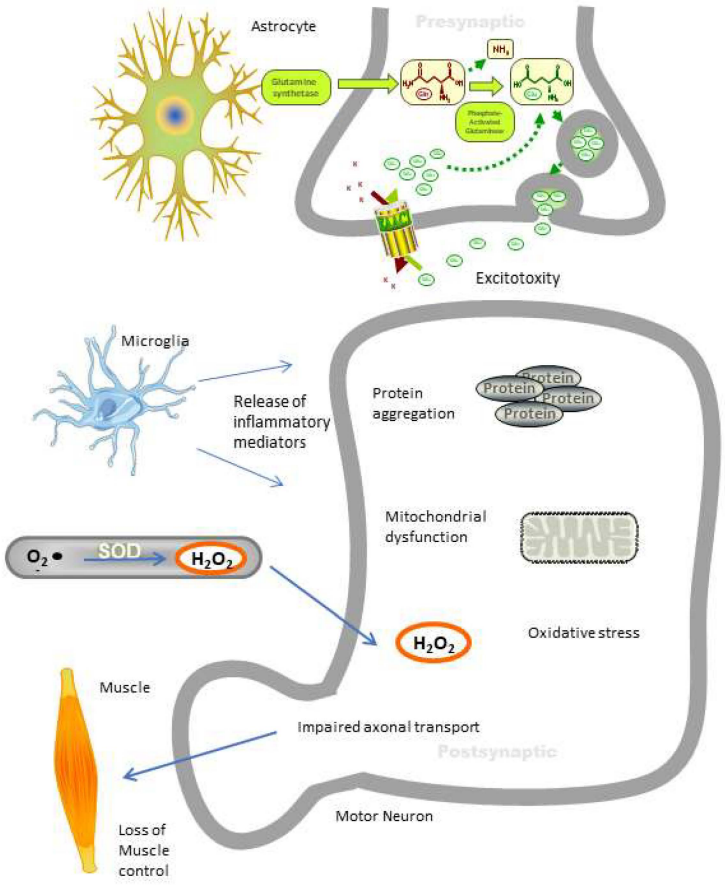

Figure 2-5 Summary of MND mechanism hypothesis.

2.2.4 Monocytes function in Neuroinflammation of MND

Neuroinflammation is a hallmark of neurodegenerative disease, which involves the activation of several immune cells, such as microglia, macrophages, and T cells. These immune cells belong to the innate immune system; their roles include secretion of cytokines for immune cell recruitment to the site of infection, clearance of cellular debris, phagocytosis of pathogens, and antigen presentation. [188]

Microglia (embryonically-derived macrophages) are reported as the essential immune cell type involved in neuroinflammation since they are the resident macrophages of the CNS.

[189, 190] Microglia are commonly believed to originate from peripheral mesodermal (myeloid) tissue, and microglial progenitors migrate into the nervous system primarily during embryonic and fetal periods of development. [191] It is widely accepted that activated microglia are a vital feature of neuroinflammation in the CNS. However, more recent studies have shown that peripheral monocytes are also involved in several neurodegenerative diseases; several changes are observed in these monocytes, such as functional alterations skewed towards a pro-inflammatory state, and invasion into the CNS. [139, 192-196]

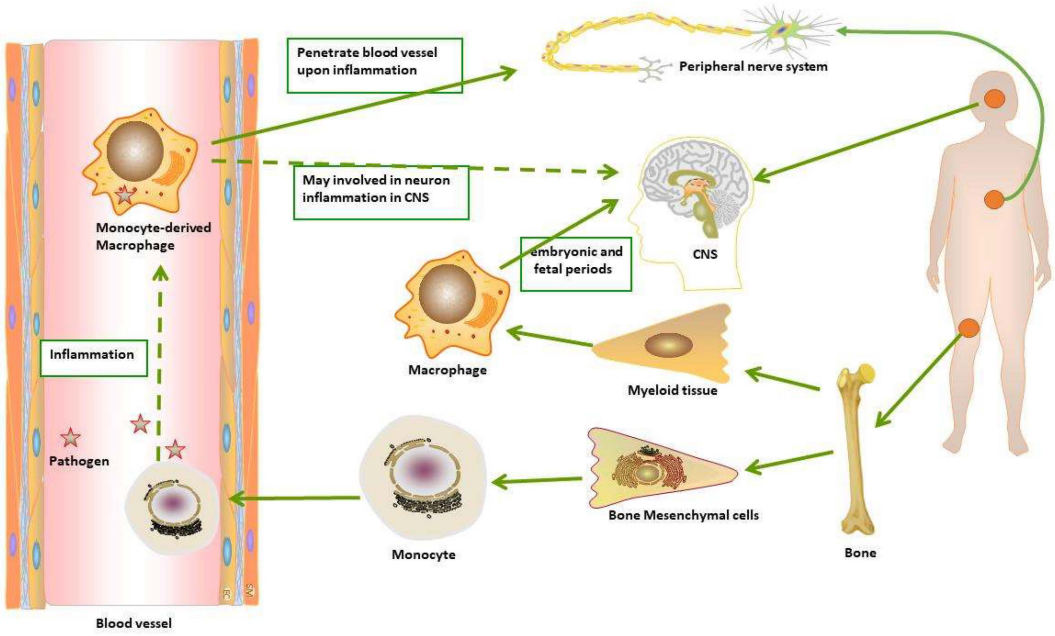

Figure 2-6 Potential role of monocyte and macrophage in MND.

Monocytes are derived from hematological precursors in the bone marrow and then migrate into the peripheral blood. [197] Monocytes have two functional subpopulations: one is believed to 'patrol' within the blood vessel, the other one is thought to respond to designated signals and penetrate the endothelium to enter the tissue. [198] Upon injury or inflammation, monocytes synthesize and secrete inflammatory mediators, and generally gain the properties similar to macrophages. These changes include enlarged cell size, changes in the mitochondria, reticulum, and lysosomes. [197]

It has been proposed that changes in monocytes within the blood may reflect neuroinflammation. For example, it is reported that upon motor neuron injury, changes in

monocyte receptors, cytokine secretion, and monocyte recruitment into CNS are observed [138, 141, 194, 199].

According to the previous discussion, monocyte can act as a biomarker for MND classification, due to its relationship with several mechanisms that exist in MND patients, as shown in **Figure 2-6**.

This study is aimed at investigating the possibility of using autofluorescence features as a biomarker for MND diagnosis. It might be possible to use the change of monocytes' autofluorescence signal to reflect the condition of the MND patients.

Chapter 3: Methodology and material

In this chapter, I am going to introduce the sample preparation procedure (monocyte isolation), HSI system setting, imaging protocol, image processing methods, information extraction methods, and data analysis methods. The sample preparation and HSI imaging were performed by Dr. Ayad Anwer and Dr. Sinduja Subramanian. And I carried out the imaging processing, data analysis, and further discussions.

3.1 Monocyte isolation

The monocyte was extracted from 15 samples, with 12 patients and three controls. All Monocytes isolation, purification, and characterization procedures were performed by Dr. Ayad Anwer and Dr. Sinduja Subramanian at the Department of Clinical Medicine Faculty of Medicine and Health Science, Macquarie University. The ethics approval is approved by Macquarie University MND biobank, Biobank HREC Number 5201600387. Monocyte isolation was performed using MACS Prep PBMC isolation kit (Miltenyi Biotec, #130-115-169,) and pan monocyte isolation kit (Miltenyi Biotec, #130-096-537). Anticoagulated Whole blood was collected in 6 ml EDTA (BD bioscience, # 367873) from ALS patients and healthy volunteers following informed consent. The samples were obtained from the Macquarie University Neurodegenerative Disease Biobank, Macquarie University, New South Wales, Australia. Full blood count was performed with 2 ml blood using the Sysmex automated hematology analyzer in Douglass Hanly Moir Pathology. Monocyte isolation was performed in 4 ml of whole blood by the negative selection procedure. Initially, PBMCs isolation was performed using MACSprep PBMC isolation Kit by the negative depletion of non-PBMCs where all non-PBMCs were indirectly magnetically labeled with a cocktail of biotin-conjugated monoclonal antibodies against CD15, CD61, CD66b, and CD235a as a primary labeling step followed by the additional labeling with MACSprep Anti-biotin monoclonal antibodies conjugated with Microbeads as a secondary labeling. The magnetically labeled non-PBMCs (e.g., neutrophils, eosinophils, platelets, and erythrocytes) were depleted by retaining them within a MACS column in the strong magnetic field of the MACS separator while the unlabelled target cells (PBMCs) were collected.

From the obtained PBMCs, human monocytes were isolated again by negative depletion of non-monocytes (negative selection) where non-monocytes were indirectly magnetically labeled with a cocktail of biotin-conjugated monoclonal antibodies followed by labeling with anti-biotin Microbeads. The non-monocytes (e.g., T cells, B cells, NK cells, and dendritic cells) were depleted by retaining them on the MACS column in the magnetic field of the MACS separator, and the unlabelled monocytes were collected after passing through the column. The obtained monocytes were washed with phosphate-buffered saline (PBS) and counted using countess II (Life technologies). Finally, 1 x 10^6 cells were obtained, which was 50% yield recovery from the initial 2 x 10^6 Monocytes. The live monocytes of ~4 x 10^5 cells were then used for hyperspectral autofluorescence imaging, where 8 – 10 fields/images per sample were captured for analysis. Monocytes autofluorescence images were also obtained from Zeiss confocal microscopy at excitation/emission of 495/519 nm with the laser set at 488 nm.

The monocytes were then stained with 1 µL LIVE/DEAD Fixable Near-IR Dead cell stain to determine the viability of cells prior to fixation, where it preserves the staining pattern by binding to the intracellular amines. The reactive dye has an excitation maximum of ~633 nm with the emission of ~750 nm. This was followed by the additional labeling with 2 µL CD14-FITC and CD16-PE (Miltenyi Biotec) and washing with 1 mL MACS BSA buffer (Miltenyi Biotec) before fixation with 2% paraformaldehyde. The purity of the isolated monocytes was analyzed using a flow cytometer (BD LSR Fortessa X-20). The gate was set around $CD14^{++}CD16^{-}$, $CD14^{+}CD16^{++}$, and $CD14^{++}CD16^{+}$ monocyte population to exclude cell aggregates and debris where ~90% monocyte purity was achieved from ~93% live cells. Qualitative analysis of monocyte purity was also done using Zeiss confocal microscopy by capturing brightfield, CD14-FITC at 495/519 nm, and CD16-PE at 545/566 nm.

3.2 HSI system setting

The basic structure of an HSI system is very similar to a conventional microscope; in most cases, they are modified from a commercial fluorescence microscope or confocal microscope [200-202]. In my research, a single photon microscope (Olympus IX71 inverted microscope) is employed, because it has several access ports for multiple inputs or output devices, such as the EMCCD camera and illumination fiber bundle and homogenizing system [108].

3.2.1 Microscope

The Olympus IX71 system can accommodate multi-wavelength, advanced fluorescence techniques [203]. It has external power supplies for better thermal stability, differential interference contrast condenser, and the capacity to house six epifluorescence filter cubes. In this study, I use the Olympus IX71 system equipped with the UIS2 optical system that can detect near-IR wavelengths, which has much lower phototoxicity, which is preferred for imaging of live cells. Besides, it also has a good performance in the conventional visible spectrum. This system has high SNR and flat, high transmittance in a wide spectrum, even in the UV range. These features are ideal for the detection of weak autofluorescence in low light conditions [203]. The schematic diagram of hyperspectral hardware set up sees **Figure 3-1**.

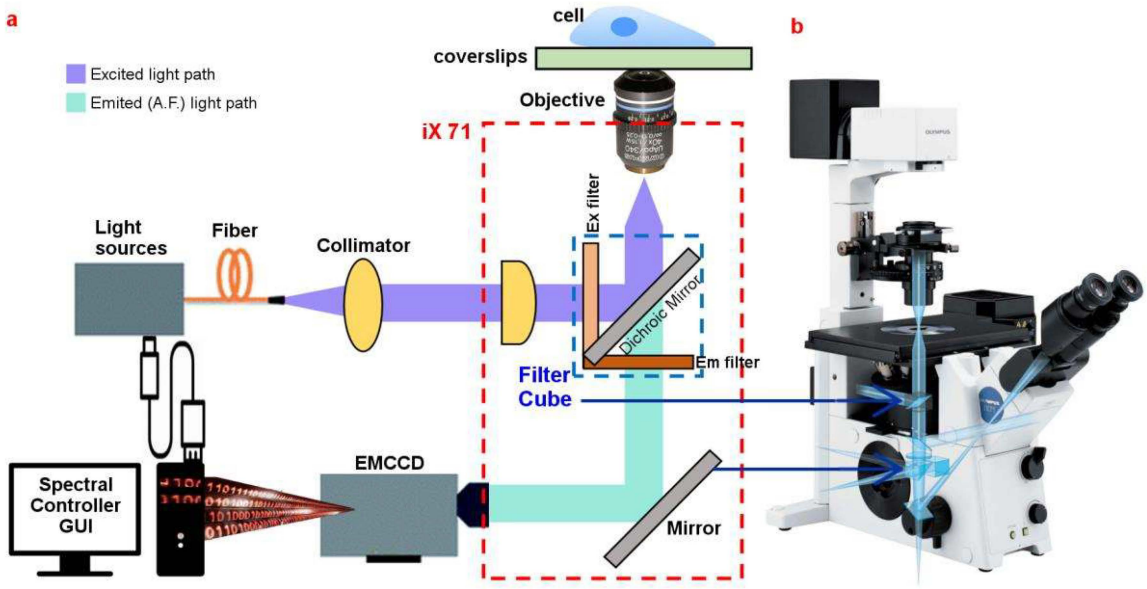

Figure 3-1 (a) Schematic diagram of the Hyperspectral hardware setup, Olympus iX71TM microscope is marked with a red dotted line, whether filter cube is spotted with a blue dotted line, (b) single-photon autofluorescence microscopy, Olympus iX71TM. Images are taken from [204]

3.2.2 Light source

Technological advances in LEDs make them viable sources for use in fluorescence microscopy. They require minimal stabilization time, have a long life, are low cost, can be obtained with narrow bandwidths in the order of 25 nm, and are available from the UV to

the green spectrum at reasonable power outputs of tens of milliwatts (mW). The LEDs available at the time of this project can provide useful outputs to record the cell's autofluorescence. Figure 3-2 shows the fluorescence intensity across a broad spectrum of excitation. In this figure, 12 LEDs are adjusted in excitation intensity with regard to the cell's autofluorescence. Here, the corresponding LEDs are presented with their actual visible color code (except the deep UV LEDs), while maintaining their full width half maximum (FWHM) characterization. Here all 11 LEDs have an FWHM width of 10 nm, except the 334 nm excitation source from a mercury arc lamp. Deep UV excitation at approximately 334 nm was provided by the use of a mercury arc lamp coupled into a fused silica fiber using a lens, and narrowband filter centered at 340 nm with 25 nm width. This captured the natural 334 nm peak present in mercury arc lamps [8].

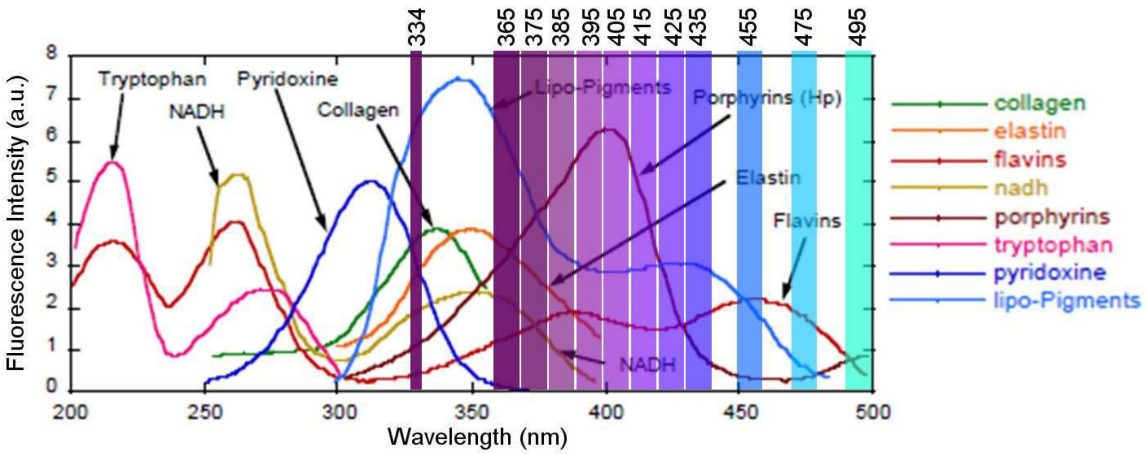

Figure 3-2 Excitation range of autofluorescence in response to different wavelength stimulation from the light source. Images are taken from[204]

3.2.3 Fiber coupling

The LED sources, laser, and mercury arc lamp emissions were all coupled into the microscope using a custom-designed bundled fiber optic cable to produce a homogeneous light source. The end of the bundle was terminated with a 5 mm fused silica hexagonal homogenizing rod[108]. The homogenizing rod employs internal reflection to turn non-uniform light sources into uniform sources, altering the spatial distribution of the pattern of origin. The particular rod employed can homogenize multipoint sources regardless of spectral characteristics.

The bundle was explicitly designed to allow multiple sources covering mid UV to near infra-red. The system requires no moving parts, and can all be TTL (transistor-transistor-logic) controlled as each LED is powered by its own current source driver module similar to the 532 nm laser module. The mercury lamp was enclosed in a ventilated enclosure and equipped with a mechanical shutter capable of withstanding the considerable heat generated in proximity to the arc lamp; this was powered by a solenoid and a TTL controllable current amplifier [108]. **Figure 3-3** gives an overall idea about the Coupling System design.

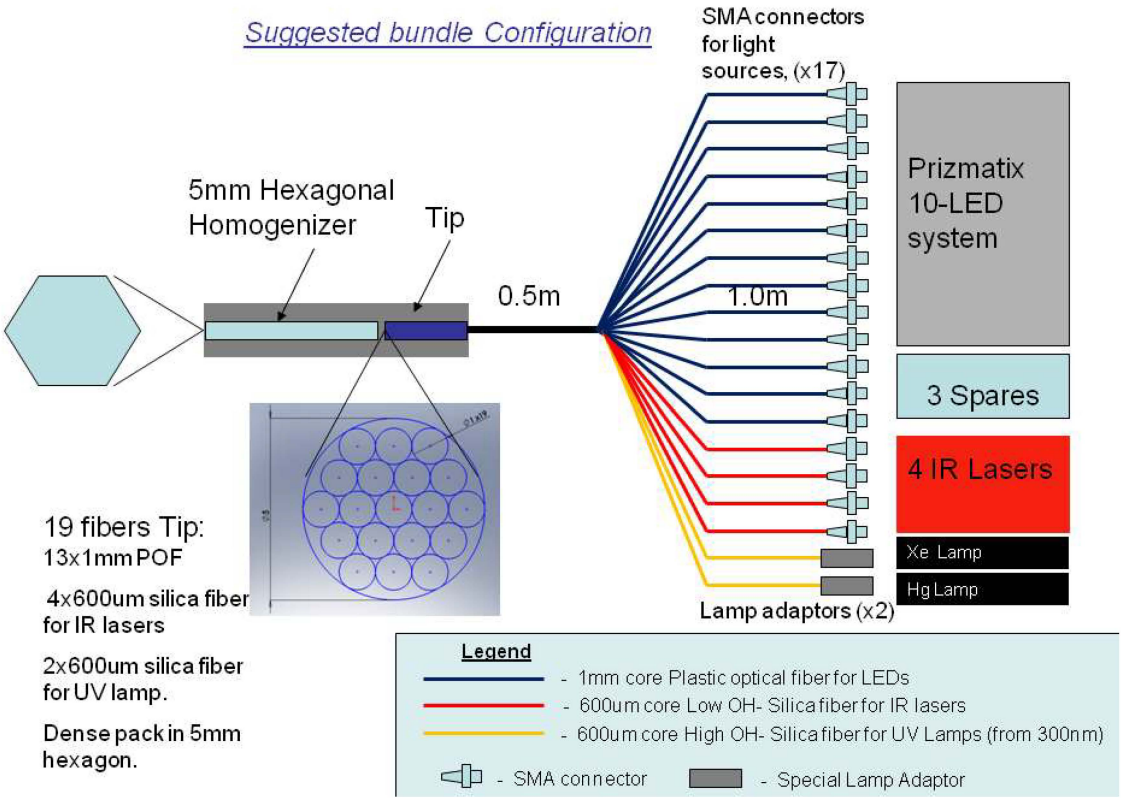

Figure 3-3 Coupling System designed to interface all light sources to the microscope with a uniform field.

3.2.4 Filter cube

Three filter sets have been employed for this project, designed by Dr. Martin Gosnell [108]. These three filters are suitable for the autofluorescence measurements from the monocyte's organelle because they can measure most of the important fluorescence emitted by fluorophores that are involved in cell metabolisms, such as NADH/NADPH, FAD, and FMN. These filter cubes use the standard epi-fluorescent configuration of a source filter to

constrain the excitation band, a dichroic, and a bandpass with excellent stopband rejection so that the camera only sees the autofluorescent emission at the shifted wavelengths.

Figure 3-4 shows the schematic filter position concerning the cell's autofluorescence emission. Both filter 1 and filter 2 use the bandpass filter for the emission, but filter 3 has a long-pass filter for emission.

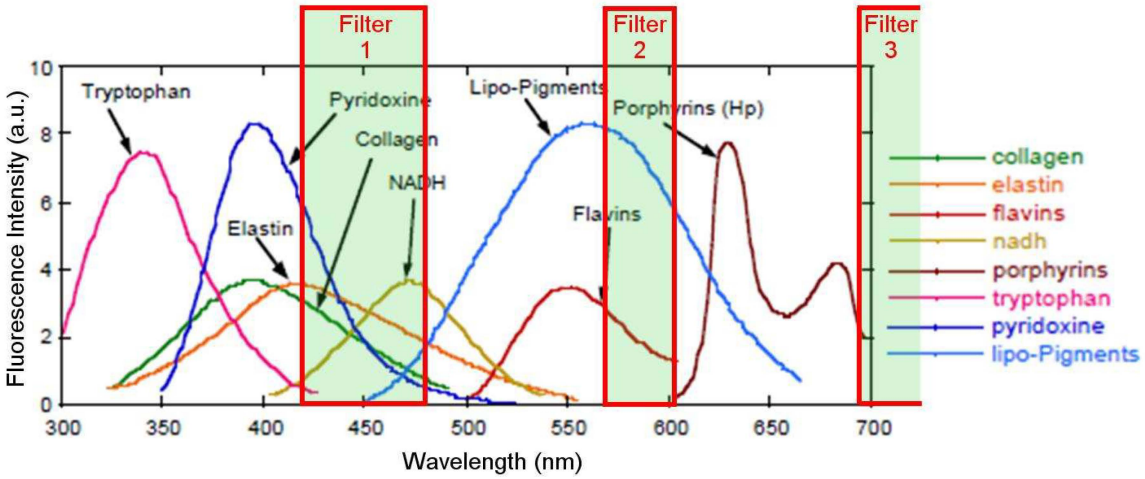

Figure 3-4: Emission range of autofluorescence detectable through the specified filter specifications. Images are taken from[204]

3.2.5 Channel set-up

It is possible to have 36 channels from the twelve illumination sources and three emission sources. However, not all the channels are useful due to the Stokes shift phenomenon of the adsorbate. As an example, it is quite unusual to find emission (i.e., Stokes shift) at 700 nm for a peak excitation lower than 400 nm. For that reason, a total of 20 channels are useful for comparing the cell's autofluorescence [203].

The specification for each channel is shown in **Table 3-1**.

Table 3-1 The list of spectral channels and the respective specification.

Spectral channel number	Excitation wavelength ±5(nm)	Emission wavelength ±5(nm)	Camera Quantum efficiency (QE) (unitless) [204]
1	365	414	0.5
2	375	414	0.5
3	334	450	0.5
4	365	450	0.65
5	375	450	0.65
6	334	570	0.65
7	365	570	0.65
8	375	570	0.65
9	385	570	0.65
10	395	570	0.65
11	405	570	0.65
12	415	570	0.65
13	425	570	0.65
14	435	570	0.65
15	455	570	0.65
16	475	570	0.63
17	495	570	0.63
18	405	700	0.63
19	455	700	0.63
20	495	700	0.63

3.2.6 Camera

In this study, an Andor iXon™+885 EMCCD camera (see **Figure 3-5**) has been used for all the sample image acquisition. This EMCCD camera is widely used in biological research [205-211] because of its superior sensitivity and reasonable SNR in low light conditions (when the signal is less than four-photon counts per pixel) while comparing to other EMCCD cameras [209]. The EMCCD camera provides a clear field of view and excellent resolution, which offers excellent imaging ability for cell microscopy, due to its megapixel sensor format and 8 × 8 μm pixel size. Even at low-light conditions, the EMCCD gain can still maintain a high frame rate at 31 frames/sec on full resolution. [204] And the EMCCD gain can be switched off when the light from the specimen is sufficient, which will improve the SNR. Besides, its extended red QE response makes it ideal for popular red-emitting fluorophore imaging.

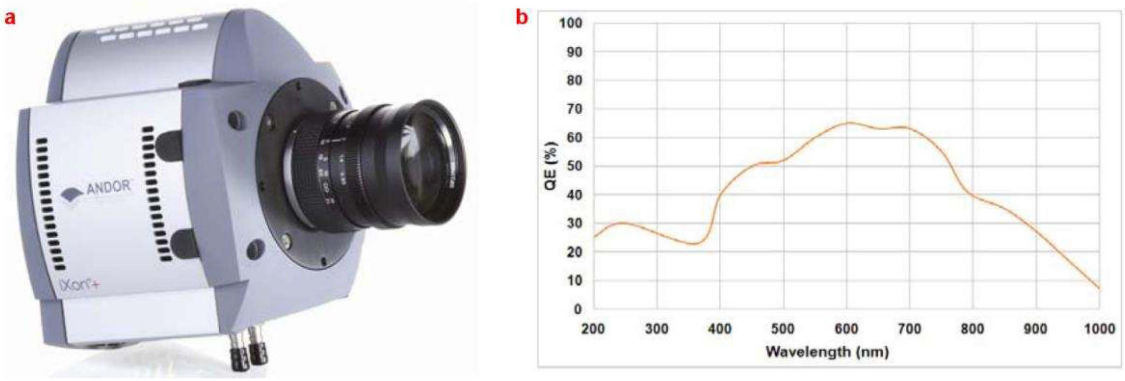

Figure 3-5 (a) Andor iXonTM+885 EMCCD, (b) Quantum efficiency of Andor iXonTM+885 EMCCD. Images are taken from[204]

Moreover, this camera is capable of detecting single photons [204]. To reduce the noise in low light conditions, the acquisition conditions are full resolution and max frame rate (35 MHz readout; frame-transfer mode; 1 μs vertical clock speed; ×1000 EM gain; 30 ms exposure; -85°C) [108]. It is essential to realize that sufficient cooling is required so that there is significantly less than one event per pixel on the EM gain.

The critical specifications for Andor iXon885 EMCCD are given in **Table E-1** in the appendix [204].

The Andor™ IXON camera captures all the images under these illuminations, and the camera operates below -65 ℃ to reduce any kinds of sensor induced noises (e.g., Illumination dependent and independent noises).

3.3 HSI imaging protocol

3.3.1 Using glass-bottom Petri dishes for imaging

The glass-bottom dishes (Catalogue Number: GBD00004-200) are made with German optic cover glass and non-toxic adhesive [212] from Cell E&G™. The dishes were sterilized with Gamma radiation. These dishes are suitable for cell culture and live-cell imaging. These are 35 mm glass-bottom dishes with 18 mm well and 1.5 German cover glass. The actual thickness, confirmed from the manufacturer, was 170 μm (±5 μm). The thickness of the coverslip is significant for high-resolution microscopy. Typical fluorescence microscope objectives are designed for use with No: 1.5 coverslips (0.17 mm thickness).

Figure 3-6(a) shows the glass-bottom Petri dishes from Cell E&G™. After that, 10 × 10 grids are etched from the inside of the Petri dishes. A femtosecond laser performed the etching at the OptoFab, Macquarie University. All the grids are designed with 400 μm × 400 μm with a specific number. This numbering is used to refer to the actual imaging area. **Figure 3-6** (b) shows the grid template. With 40 × objective, typically a 190 μm × 190 μm area is imaged. Thus 400 μm × 400 μm gives enough space to image the center of a specific grid without interference with any grid line or number. (the grid lines are around 10 μm wide, and a single digit is 20 μm wide in this template) . After etching, the glass bottom dishes are soaked and washed with laboratory glassware detergent and a 10% bleach solution. Then the dishes are washed three times, with 70% isopropanol to sterilize. After that, all the dishes are air-dried in class II sterile safety cabinet and irradiated with UV for another 30 minutes for further use.

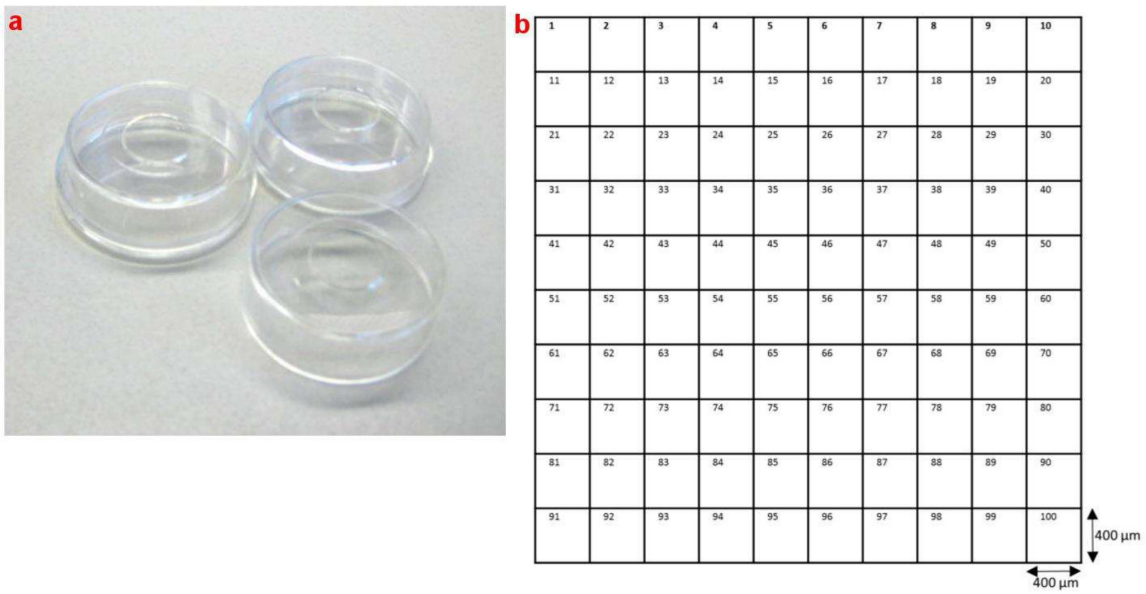

Figure 3-6 (a) glass-bottom Petri dishes from Cell E&G^{TM}, (b)Schematic design of etched grid

3.3.2 Media exchange to non-fluorescent medium

Before any cell experiment, all Petri dishes containing cells were washed thoroughly for at least three times with Hanks balanced solution (HBS), where HBS is a non-fluorescent medium. Then each small petri dish is rinsed with 1 ml HBS before imaging.

3.3.3 Hardware checking

At first, the physical connection of the EMCCD camera is checked for the link with the C-mount camera port tube (U-TV0.63XC) for the alignment purpose. Otherwise, the EMCCD's data will not be transferred properly to the P. After that, the fluorescence turret (IX2-RFACEVA) with appropriate filter cubes (filter specification is given in Section3.2.4) is installed for imaging. If any of the power or data cables are not plugged properly, it is needed to restart the whole system again. In our setup, the hyperspectral cables are not necessary to be connected. Because the EMCCD usually controls through customized Matlab software. This software controls the light sources through the 24 channel digital I/O card (USB-1024LS), stored the digital counts for the images as HS data cube. Moreover, other parameters are sorted with another specific description file.

3.3.4 Using data acquisition GUI to take images

The data acquisition GUI is operated in the MATLAB command window; this data acquisition GUI runs by writing the command of spectralControllerGUI. Details of the data acquisition GUI operation specification refer to Appendix section F.

3.3.5 Taking references images

As mentioned before, two sets of reference images are taken, water images and calibration images.

Calibration fluid is essential for calibration procedure, and it is a combination of dissolved fluorophores that would generate a spectrum that can be detected on an excellent signal level at all wavelengths within the current existing channels. Since every fluorophore has its unique, but uneven spectrum throughout the channels of interest. This is impossible to produce an even spectrum with good SNR using one fluorophore due to their different quantum efficiency at different wavelengths. Moreover, different signal power from the light source makes it more difficult. It is also important to notice that fluorescence intensities are corresponding to the concentration over only a limited range of optical densities of the sample, and this linear relationship is easily affected by the fluorophore content from the sample. However, a linear correlation is preferable between the concentration of fluorophores and the intensity of the fluorescence, and it means we need to control the concentration of each fluorophore precisely. It is reported that a mixture of fluorophores at certain concentrations can provide a roughly flat spectrum throughout all wavelength[108], which means, the flattest spectrum will have better photon counts and a decent SNR (signal to noise ratio throughout all channels).

Water images served as background images for subtracting the background autofluorescence that might come from other sources. These images are later used for correcting the ununiform illumination from the light sources.

3.3.6 Taking the sample image

Once the sample has been prepared and place into the imaging dish, the image of the sample can be taken following the same procedure of taking the reference images, and some parameters need to be adjusted according to the different features of each sample in order to optimize the contrast and brightness. Two differential-interference-contrast microscopy

images (DIC images) were also taken for cell segmentation purposes, and this procedure was used to mask the cell area in the images. Images for different channels were taking by changing the light source and change of the filter cubes.

3.4 Image pre-processing

All the information in raw hyperspectral images is stored as photon counts. However, photon count is not a comparable unit for pixel values from different channels, because it is highly dependent on the quantum efficiency of the camera, exposure time, camera sensitivity, and EM gain, and all these parameters differ from channel to channel. All pixel values are therefore converted into a standard unit, PPS (photons per pixel per second), to perform further image processing operations, such as background subtraction, nonuniform illumination correction, and image smoothing. All these operations, including PPS conversion, are dealt with in the pre-processing procedures.

In our system, PPS calculation for the camera (Andor iXON™) is given in Equation **3-1**

$$y_{raw|PPS|}(k,e,f) = \frac{(y_{raw|digital|}(k,e,f) - BO_{|digital|} \times se)}{G_{EM} \times QE \times t_{expo}} \quad \textbf{(3-1)}$$

Here $y_{raw|digital|}(k,e,f)$ denotes the arbitrary unit for digital counts (at the range of 2^{14}) for the sample, where k stands for channel number, e,f stand for the spatial coordinate of the pixel and the Bias Offset, $BO_{[digital]}$. Here $BO_{[digital]}$ is 100 counts for this experimental setup. Moreover, the sensitivity (se) for the readout rate at 13 MHz is 0.89. The EM gain (G_{EM}) and exposure time (t_{expo}) are adjusted by the operators individually for different channels, according to several factors, such as camera quantum efficiency, filter transmission rate, and the property of the sample [213]. The quantum efficiency (QE) of the camera detector is different for each channel (see **Table 3-1**).

Due to the high sensitivity of the EM gain sensor, accompanied by abnormal behavior from sensor pixels, random noise like spikes or dips is easily generated in the images. To minimize the effect of noise, a median filter with a size of 3 × 3 pixels is applied to the images. The median filter is designed to remove abnormal pixels with extreme value compared to its neighborhood. The size of 3 × 3 pixels is chosen for the median filter, to make sure the filter only removes the abnormal pixels itself without blurring the image.

The EMCCD camera's main noise sources are split into two broad classifications, light-independent noise, and light-dependent noise [107]. The illumination-independent noises (including dark-current shot noise and readout noise) are temporal noise, which is affected by temperature changes. This noise can be minimized by using optimum temperature (below -65°C) [214]. Illumination-dependent noises (including clock induced charge noise, photon shot noise, and EM gain register noise) are a combination of temporal and spatial noise. This illumination-dependent noise is considered additive Gaussian distributed, and usually minimized by image pre-processing methods [108].

Except for autofluorescence from the biological sample, there is also unavoidable autofluorescence signal from microscope slide, Petri dishes, dirt on sensors, or some ambient light sources [214]. These make up a background signal across the field of view. To remove this background noise, I took three hyperspectral images of water solution in the petri dish used for imaging [108]. The average of these images was smoothed and designated as $B(k; e; f)$, which was different for each channel, and later used as background subtraction images.

Then a `calibration fluid' is prepared for calibrating the HSI system. The calibration fluid is made of 30 μM NADH and five μM riboflavin[109], which has a spectrum of non-zero response through all our spectral channels. The calibration fluid image is also smoothed to avoid an exaggerated result, and denoted $C_{raw}(k; e; f)$. The excitation and emission spectra of our calibration fluid were also measured at a specific channel using a Cary Eclipse Fluorescence Spectrophotometer™. The spectrum is then normalized to a sum of 1 across all channels and designated as p(k). This spectrum was then used to correlate the hyperspectral images with fluorescence spectra. This step is essential for correctly assigning the unmixed fluorophores by using the spectra of reference pure fluorophores for the future unmixing purpose. The hyperspectral imaging system was then calibrated by subtracting the water images from both the calibration fluid image and sample images; this was done by subtracting the pixel values of this smoothed water image from each calibration fluid and sample image in the hyperspectral data cube.

Finally, the calibration fluid images and water images were also used to correct the uneven (approximately Gaussian) illumination of images [214]. In previous researches done by our group[8, 81, 109, 117, 126, 215, 216], the uneven illumination correction was done by dividing background-subtracted sample images in each channel by the related background substracted calibration fluid images, each of them having been smoothed by Wavelet filter.

[8] The relationship is illustrated in equation **3-2**, where $y_{raw}(k; e; f)$ stands for the 2-D raw images, $B(k,e,f)$ is the water image, $C(k,e,f)$ is the calibration fluid, and p(k) stands for the normalized spectrum.

$$y(k,e,f) = p(k) \times \frac{y_{raw}(k,e,f) - B(k,e,f)}{C_{raw}(k,e,f) - B(k,e,f)} \quad \textbf{(3-2)}$$

3.5 Cell segmentation

In this research, the cell segmentation procedure was performed manually based on the DIC images. Because the autofluorescence signal is different from each channel, and each channel may cover different areas of the cell, only a combination of all masks from all channels can potentially provide more reliable results. However, due to the lack of sufficient automatic segmentation methods, it is impossible to segment all the fluorescence images manually. Giving that the autofluorescence signal near the membrane will be blurry and hard to determine a cut-off value manually, it is more reasonable to conduct this process based on DIC images. These images have a consistent optical feature through all the samples, and they usually have a more definite boundary than fluorescence images. After taking all these elements into account, the masks are drawn near the shadow of the cell from the DIC images. (See **Figure 3-7** for example). The consistency of the manual segmentation is also evaluated later.

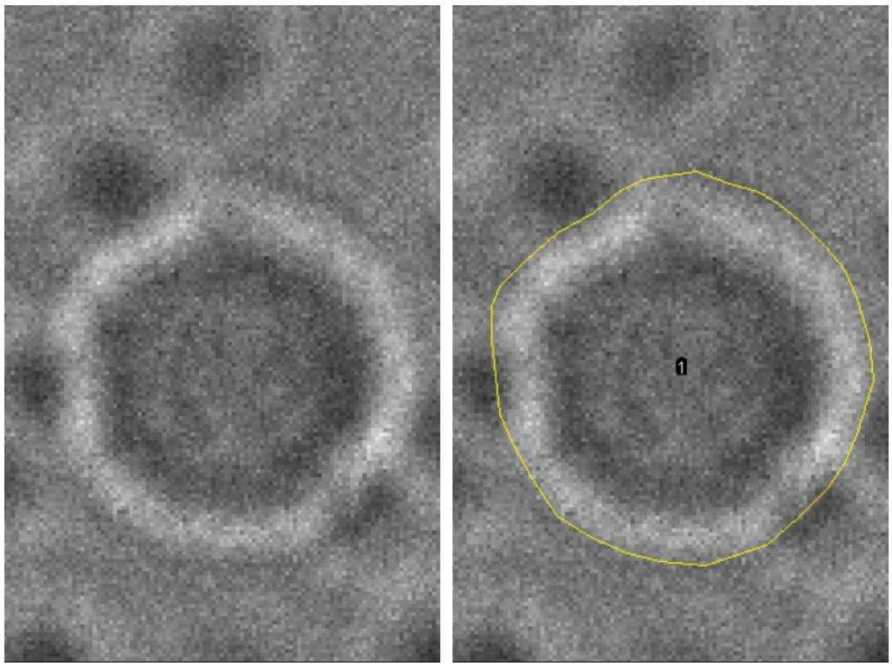

Figure 3-7 Manual segmentation. A) Original image. B) The yellow line shows the boundary of the mask

3.6 Information extraction

After segmentation was finished, all pixel values (measured in PPS) within the masks are extracted from the original image, and all pixel values were assigned to their related cell label for further analysis. For each cell, the measurements include mean pixel value for each cell (PPS per pixel, designated as M_{SN}, where SN stands for the cell number from a specific sample), and for each sample, the measurement is the mean PPS value (PPS per pixel, designated as M_s, where s stands for the sample code). It is shown in **Figure 3-8**.

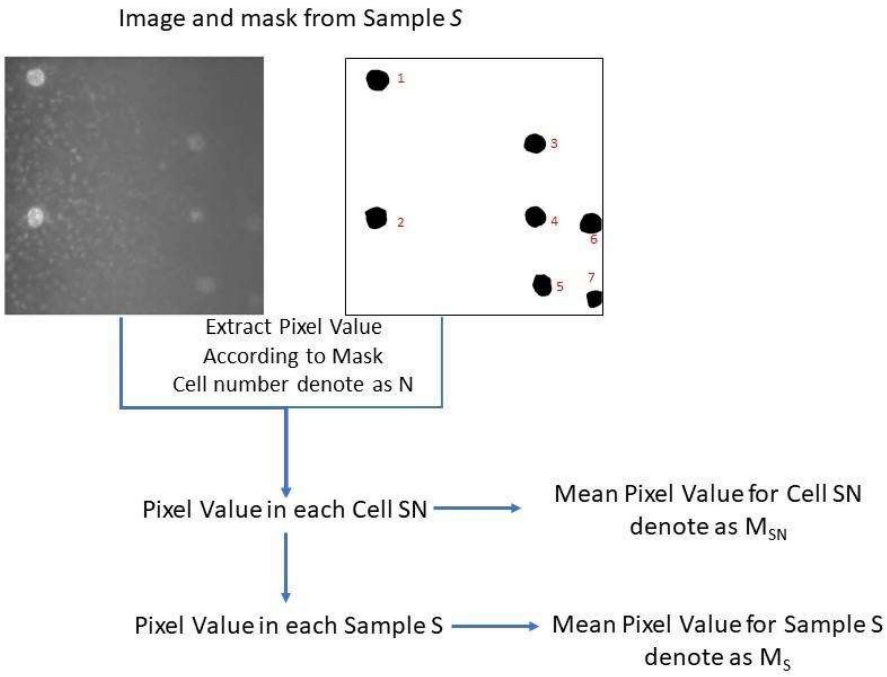

Figure 3-8 Information extraction procedure

Because of the low SNR from specific channels (Channel No. 3,6,18,19,20), images from these channels were discarded. Otherwise, these noisy channels would introduce significant errors to subsequent analysis.

3.7 Data analysis

3.7.1 Classification

In order to find the simplest way to distinguish patient samples and control samples, I presumed that there is one particular channel could be used to classify the two sample groups. So I employed the single-channel analysis to see whether this channel exists. In this analysis, M_s was used to compare the differences between each sample across all samples in each channel. And the channel with a significant difference between the two groups can be used for the classification of samples. Kruskal–Wallis tests were applied to exam the significance. Differences were considered significant if $P< 0.05$.

However, this analysis is unlikely to work successfully, so more complex analysis will be required. And these analyses will be based on the features extracted from the channel information. In order to determine which channels are more likely to help me distinguish the

two groups, principle component analysis (PCA) [217] was employed. In this study, PCA is used as a dimension reduction tool to extract the best principle component that could be used to classify the samples. Each principal component represents a mix of a portion of certain channels. PCA is applied based on M_s data in order to perform dimension reduction. Then a selection of channels will be used as features for further analysis depending on the results of the principal component analysis, and their biology is meaning. An unsupervised classification method named cluster analysis is performed to distinguish the two groups.

3.7.2 Data anonymization

Before image pre-processing began, the images were renamed randomly by a piece of MATLAB code. Each sample will be coded with a letter instead of its original file name. This information was stored in a .mat file, and it is not accessed until the analysis is finished. In this case, I have no insight into the result until I have finished my analysis. This information is included in **Table A-1** in the appendix, section A.

Chapter 4: Result and discussion

4.1 Image pre-processing

Figure 4-1 shows the effect of the Wavelet filter on the cell image preprocessing procedure accompanied by the median filter. They removed the spikes and dips in the signal caused by cosmic rays and inactive pixels, and they also preserved the signal in the region of interests.

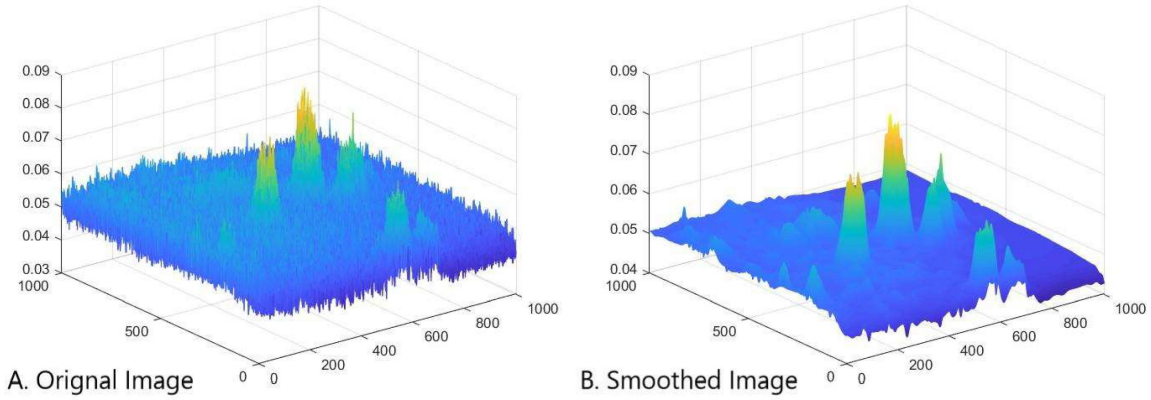

Figure 4-1 Cell Image surface plot. A. Original image. B. Pre-processed image

However, due to the poor quality of the water image, it needs to be discarded from the flattening procedure in order to eliminate the error that is introduced by it. In the final result, I only used related calibration fluid images for flattening; the new equation is used to replace equation 3-2[shown below.

$$y(k,e,f) = p(k) \times \frac{y_{raw}(k,e,f)}{C_{raw}(k,e,f)} \quad \textbf{(4-1)}$$

4.2 Cell segmentation evaluation

In this research, all cell segmentation was performed manually, although the standard was described clearly before, it is still a subjective method. To understand the error that may be introduced by manual segmentation. I repeated some of the segmentation processes on four randomly chosen groups. And then, the similarity of these two related masks was compared to evaluate the accuracy of this approach.

Figure 4-2 shows the sample mask images used to evaluate the accuracy of the similarity coefficient functions. Two similarity coefficient functions were applied for cross-validation; they are Sørensen-Dice similarity coefficient (DSC) and Jaccard similarity coefficient (JSC). The equation for DSC is shown in **Equation 4-2,** where X and Y represent the two images under comparison. The equation for JSC is shown in **Equation 4-3**. In this research, the higher the similarity functions are, the more similar the two images are. It is shown in **Table 4-1**.

$$DSC(X,Y) = \frac{2|X \cap Y|}{|X|+|Y|} \quad \textbf{(4-2)}$$

$$J(X,Y) = \frac{|X \cap Y|}{|X| \cup |Y|} \quad \textbf{(4-3)}$$

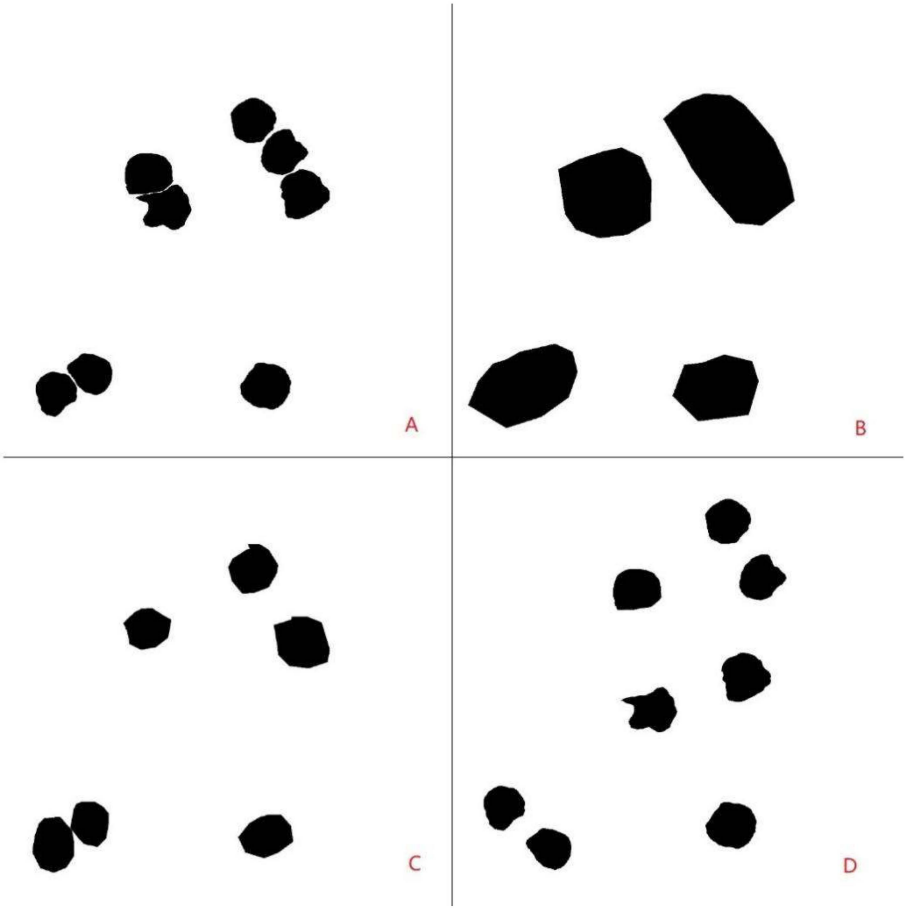

Figure 4-2 Manual segmentation evaluation method assessment. A) original mask. B) Intentional enlarged mask, C) Mask with missing cells, D) Shifted original masks

Table 4-1 Manual segmentation evaluation

Evaluation function	Intentional enlarged mask	Mask with missing cells	Shifted original masks
Sørensen-Dice similarity coefficient	0.62	0.77	0.15
Jaccard similarity coefficient	0.45	0.624	0.081

According to **Table 4-1** and **Figure 4-2**, it is clear that the masks do not only need to share the same shape but also need to be in the same location in order to gain a high score in these similarity functions. These functions are quite ideal for examing whether my manual segmentation method can be repeatable or not.

Afterward, I applied two similarity coefficient functions to some randomly picked samples; these samples were manually segmented at different times but follow the same principle. The similarity functions for the repeated manual segmented masks are then compared to see the repeatability of the segmentation. The result is shown in **Table 4-2**. The segmentation was entirely consistent with a similarity score, all over 90% accuracy.

Table 4-2 Manual segmentation consistency evaluation

Sample Image Code	Sørensen-Dice similarity coefficient	Jaccard similarity coefficient
B (1)	0.96	0.93
B (2)	1.00	1.00
B (3)	0.96	0.93
B (4)	0.97	0.94
B (5)	0.96	0.93
B (6)	0.97	0.94
B (7)	0.96	0.92
B (8)	0.95	0.90
G (1)	0.92	0.86
G (2)	0.95	0.90
G (3)	0.92	0.86
G (4)	0.94	0.89
G (5)	0.95	0.90
G (6)	0.94	0.88
G (7)	0.93	0.86
H (1)	0.95	0.91
H (2)	0.95	0.91
H (3)	0.91	0.83

H (4)	0.96	0.93
H (5)	0.92	0.85
N (1)	0.95	0.90
N (2)	0.96	0.92
N (3)	0.96	0.93
N (4)	0.97	0.94
N (5)	0.95	0.91
N (6)	0.97	0.93
N (7)	0.96	0.93
N (8)	0.95	0.91
Average (SD)	0.95 (0.02)	0.91 (0.03)

SD: Standard deviation. Each number represent an image number

4.3 Single-channel analysis

After cell segmentation was completed, all pixel values in the cell area can be extracted from the images according to the mask. Then the $M_s(CH)$ is calculated based on the pre-processed images for the selected channels, where CH stands for the channel number. It is shown in **Figure 3-8**. $M_s(C)$ is compared to every channel separately. The result shows that none of the channels can separate the samples into two clear groups, where patient samples and control samples are being separated. **Figure 4-3** shows an example of the single-channel analysis results of channel 11 using the t-test. There is no significant difference between the control group and the patient group. The other results are quite similar; see appendix section A for detail. Here sample H and J have an unusually high variance; it is most likely due to the high cell number that was measured in these two samples. (See **Table D-1** for cell numbers per sample). However, this difference in cell number per sample was mainly because of the lack of enough samples. Consider the low concentration of monocyte in peripheral blood; it is likely that the number of isolated monocytes is hard to be maintained at the same level for different samples. Besides, the imaging area was randomly chosen, eight areas were imaged for each sample, so it is hard to maintain the consistency of cell numbers in this work. In future experiments, instead of using imaging numbers to measure the sample size, it is more reasonable to image a similar number of cells for each sample for further analysis.

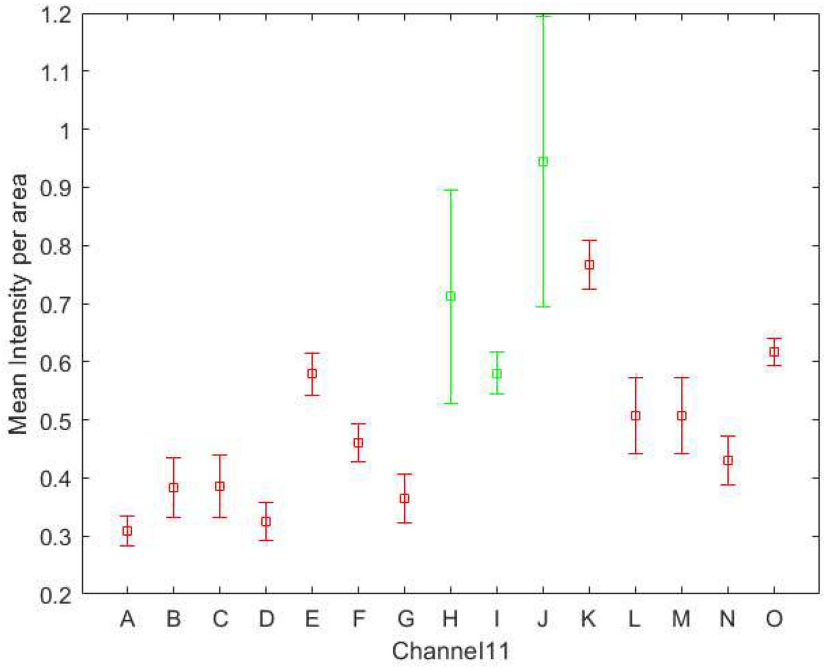

Figure 4-3 Mean cell intensity per pixel on Channel 11 Green represents control samples; red represents patient samples.

4.4 Principal component analysis (PCA)

It is as expected that single-channel analysis cannot provide us with a precise classification method, because of the complexity of biological metabolism process and their complicated relationship with the fluorophores involved. In order to extract useful features for further classification, I employed PCA on the mean intensity per cell to determine whether there would be a combination of channels that can help to distinguish the patient group and control group.

According to the scree plot of PCA (see **Figure 4-4**), the first two components were chosen for further analysis, since they explain 95.7% of the co-variability among all principal components. This proportion is calculated by dividing the sum of the variance for principal component 1 and principal component 2 (P1 and P2) by the sum of the variance of all the principal components.

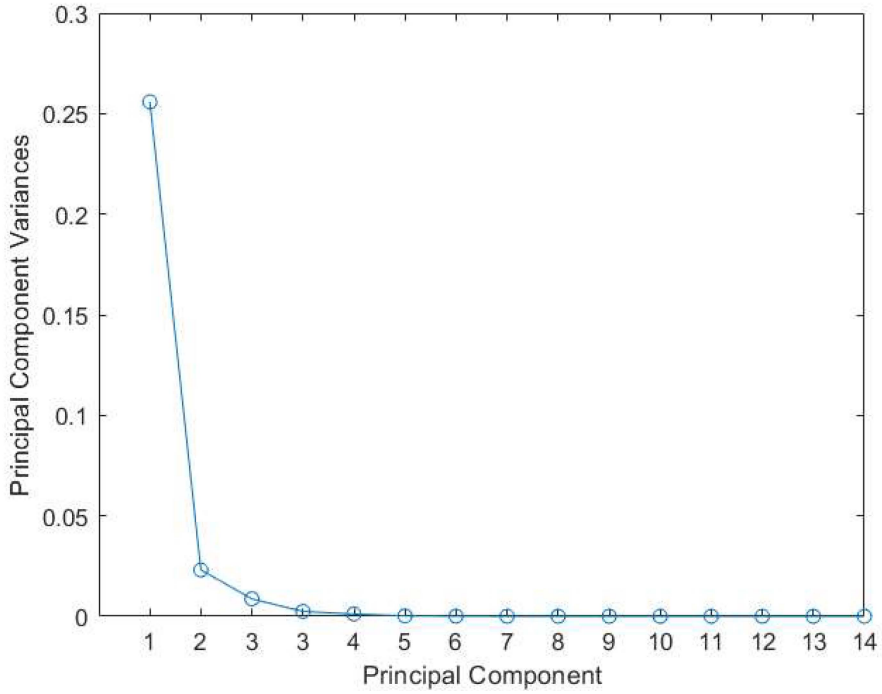

Figure 4-4 Scree plot of PCA result, it shows the variances of each principal component.

Then all the original data were converted into the principal component value by the loading matrix (**Table 4-3**) and **Equation 4-4**.

$$Pn = \sum_{C=1}^{C=20}(M_{S_C} \times L_{Cn}) \quad \textbf{(4-4)}$$

Here, P_n designated the value of principal component n; CH means channel number, M_{S_C} designated the mean intensity value for sample S in channel C, and L_{Cn} stands for the loading value for channel C in P_n.

Table 4-3 Loadings matrix of PCA for P1and P2

Variable	P1	P2
CH1	0.190	0.664
CH2	0.084	0.128
CH4	0.372	0.591
CH5	0.145	0.082
CH7	0.185	-0.097
CH8	0.174	-0.053
CH9	0.237	-0.059
CH10	0.277	-0.120
CH11	0.291	-0.139
CH12	0.316	-0.107
CH13	0.348	-0.140
CH14	0.333	-0.165
CH15	0.299	-0.187
CH16	0.260	-0.132
CH17	0.161	-0.161
CHn: stand for channel number.		

After the value for P1 and PC2 for each sample are calculated, I used clustering analysis to classify all samples into two groups in order to separate patients and controls (result in **Figure 4-5**). Although the first group (blue) are all patient samples, the second group (red) consists of 5 patient samples and three control groups. It means that using cluster analysis with P1 and P2 is not a completely accurate classification method for the sample set.

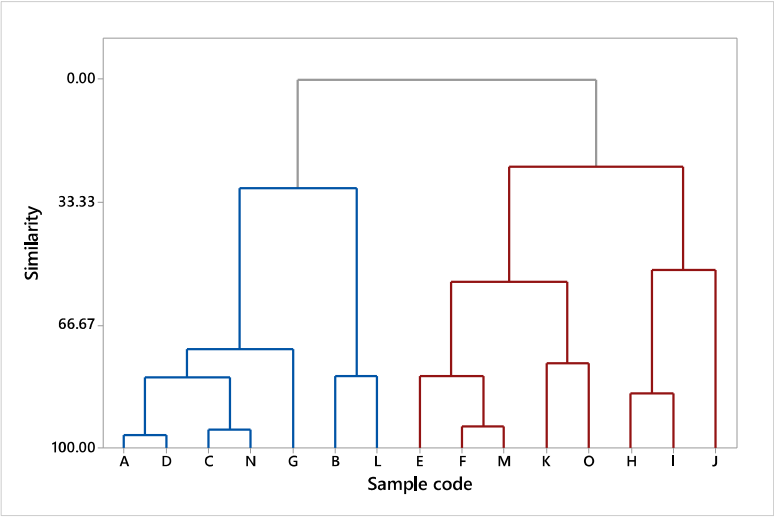

Figure 4-5 Cluster analysis result based on P1 and P2 value

In order to further examine the accuracy of classification with these two features (P1 and P2), I applied linear discrimination analysis, see **Figure 4-6** for the result. Two classes can be divided from the graph. The first one consists of the patient (B, L) and control (H, I, J), and the second one consist of all other patient samples. Although the accuracy is higher than the cluster analysis, it still only has an accuracy of 86.67%. It is unlikely to increase the accuracy any further due to the small sample set.

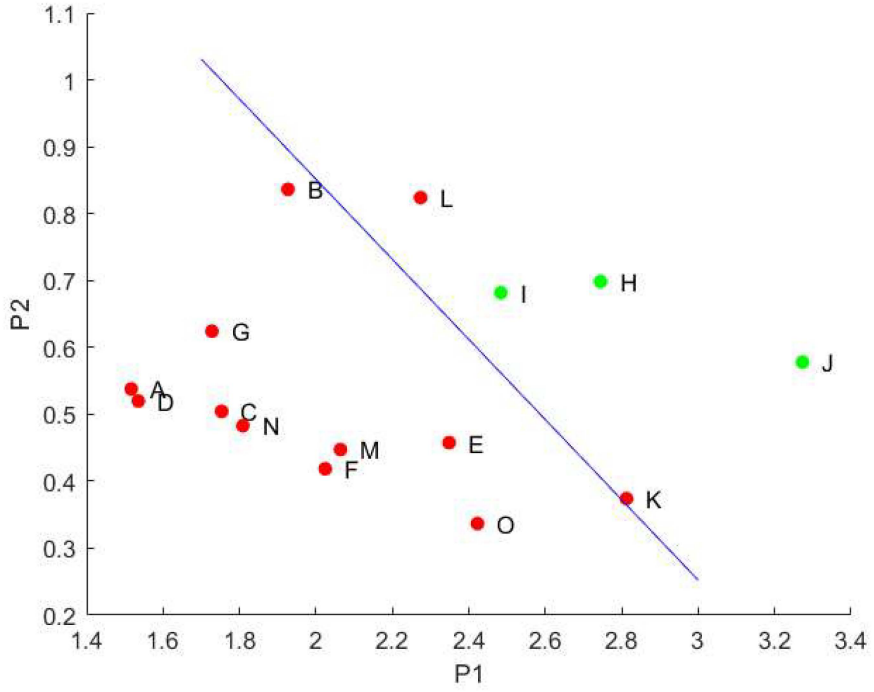

Figure 4-6 Sample plot with linear discrimination result. The line of separation is in blue.

4.5 Feature extraction

Although most patients can be distinguished from the control, the accuracy is only around 86%. Considering the small number of samples within the two experimental groups (especially the control group with only three samples), a lower accuracy is expected. What is more, it is hard to have a clear biological explanation for these principle components. Thus, the direct use of these principle components as either a biomarker or a tool to explore related metabolism mechanism seems complicated. Instead of directly using the principal component, it seems more reasonable to take the sum of the signal from specific channels according to the loading matrix. There are two reasons for doing so. First, mathematically,

the loading matrix represents how important each variable is in the PCA results. Thus, the channels with higher absolute loading values will have a more significant role in distinguishing different groups. According to the loading matrix (shown in **Table 4-3**), I think channels 5 to 16 are essential to feature 1, while channel 1 to 2 is more critical to feature 2. Second, it is necessary to take into consideration which combination of the channels would have a biological meaning. As described before, each fluorophore would have its unique spectrum across all channels. According to our previous studies, the intensity for each fluorophore distributes differently throughout all the channels. For each fluorophore, we normalize the intensity to a sum of 1 in all channels; then, we will get a normalized spectrum for each fluorophore. Based on these spectrums, we found that nearly 95% of the intensity for FAD can be measured from channel 5 to channel 16, while only around 19% intensity of NADH(NADPH) can be measured in this range. For other fluorophores, due to

$$S1 = \sum_{C=5}^{C=16} M_{S_C} \quad \textbf{(4-6)}$$

$$S2 = \sum_{C=2}^{C=1} M_{S_C} \quad \textbf{(4-5)}$$

their low concentration in cell and low quantum efficiency in these channels, their fluorescence can be considered as insignificant. In our system, it seems reasonable to assume, the change for the total intensity from channel 5 to channel 16 will mainly due to the change of FAD. The equation for the new features is shown in equation **4-5,4-6**, where S1, S2 represent two new features described before. These two new features will be an exam for their classification accuracies using both cluster analysis and LDA.

4.6 Classification method and evaluation

Using features S1 and S2 as described before and applied it with linear discrimination, it can separate the two groups with the accuracy of 93.33%. The linear discriminant function and the classification result is shown in and **Figure 4-7**.

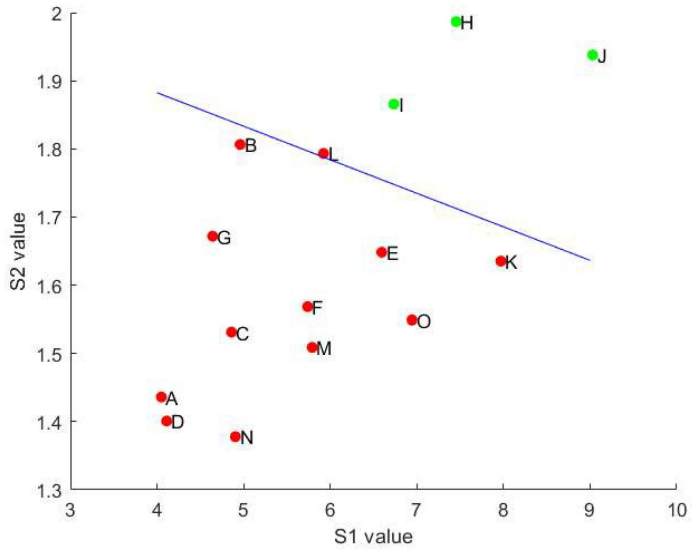

Figure 4-7 Sample plot with linear discrimination result. The line of separation is in blue.

This result from LDA indicates that S1 and S2 could potentially be two better features for classification than P1 and P2 because the accuracy for classification using S1 and S2 is higher than that of P1 and P2. In order to further test this assumption, I repeated the cluster analysis on S1 and S2. See **Figure 4-8**.

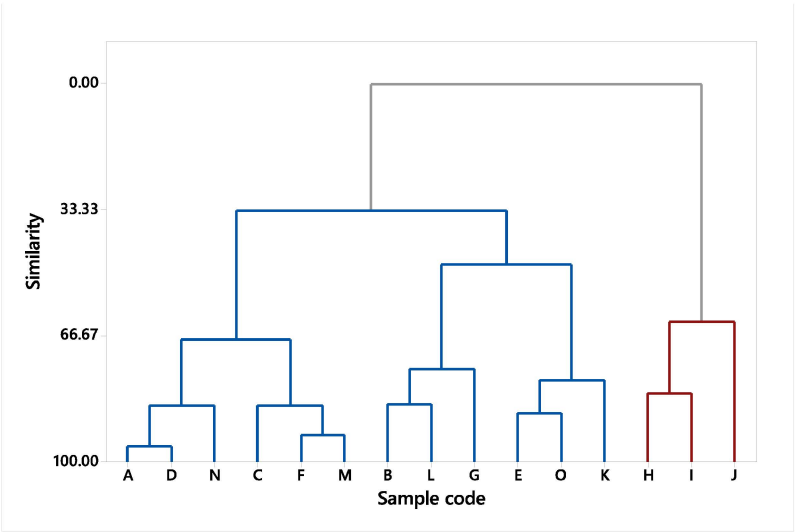

Figure 4-8 Cluster analysis result based on S1 and S2 value

It further validated the assumption that S1 and S2 could serve as two better classification features, since, they correctly classify all the samples into two groups, where they all belong to their actual group. In further experiments, with the aid of the existing dataset, it is possible to assign future samples into the correct group.

When only considering S1, it can classify most samples correctly; It may indicate that there is a change in the FAD level in the monocyte of MND patients. Nevertheless, relative biochemistry experiments need to be performed in order to validate this hypothesis.

From **Figure 4-7**, it is likely that patient samples have a lower value of S1 when comparing to control samples. It indicates that monocytes from MND patients may have a lower concentration of FAD when comparing to healthy controls. However, the mechanism behind this is still not clear. It is reported that disruption of FAD synthase may lead to a rise in the ROS level [218], and the presence of oxidative stress plays an important part in MND [180, 183, 219]. It is likely there is an increase of ROS level, and a decrease of FAD level takes place in monocyte, but the biological meaning behind this still needs further investigation.

In order to further examine the accuracy of S1 and S2 as a classification feature, I used cross-validation to estimate the accuracy of these two features using LDA. In the cross-validation simulation, I selected two samples as test samples each time and used the remaining 13 samples to calculate the linear discrimination function. Then I use these functions to exam the accuracy using the two test samples. I repeat this process for all the possible combinations and calculate the meaning accuracy, which is likely to be the estimated accuracy for these two features as a classification feature. The results show that when applying S1&S2 as classification features, it has an accuracy of 86%. Consider the small sample size, and it is quite likely the accuracy could improve with more training samples.

Chapter 5: Conclusion and Perspective

5.1 Conclusion

In this study, I have undertaken proof-of-concept studies to evaluate the utility of HSI methods as a potential classification method for MND patients, based upon autofluorescence profiles of patient monocytes isolated from peripheral blood. PCA analysis demonstrated a degree of separation between patient and healthy control samples, based predominantly upon changes in FAD autofluorescence. However, the full separation was not achieved, presumably because of the small sample size (particularly the control group). This project, therefore, provides encouraging results for HSI-based identification of MND patients based upon monocyte autofluorescence, warranting future investigation.

5.2 Perspective

For this project, I only have three control samples, and fifteen samples in total, it is impossible to reach any conclusive result. But it did gave us some impressive results.

For these MND patients, due to the lack of more detailed information, I had to assume they are similar. However, it is highly likely they could be divided into subgroups depending on genotype, disease stage, age, gender, or/and some other parameters. Some groups would be much similar to the controls, while some are not. If more clinical information were provided, it could help understand what parameters may contribute to the variances within the patient group. In future experiments, it will be beneficial if all information regarding the patient's condition is accessible. Besides, it will be constructive if we could measure the monocytes from the same patient, but in different disease stages.

For further experiments, measuring the FAD concentration after HSI imaging through relevant biochemical experiments could validate whether changes of FAD in monocytes could be used as a biomarker for MND patients classification. Or the measurements could be performed by unmixing the HSI images using a reference excitation-emission matrix of pure FAD [8]. Another solution is by fluorescence-based measurement, see [220].

From this project, there are still some improvements that need to be made for current methods. First, an automatic and constant cell segmentation software needs to be specifically developed for our HSI system. It will be more time-efficient than manual segmentation. Second, a more user-friendly interface needs to be developed in order to ease the use of the HSI system and HSI data process for users with different backgrounds. Third, it is crucial to improve the monocyte's preparation procedure so that we could measure almost the same number of monocyte for each group. It could help us improve the accuracy of the results.

Reference

1. Zimmermann, T., J. Rietdorf, and R. Pepperkok, *Spectral imaging and its applications in live cell microscopy.* FEBS letters, 2003. **546**(1): p. 87-92.

2. Goldys, E.M., *Fluorescence applications in biotechnology and life sciences*. 2009: John Wiley & Sons.

3. Broussard, J.A., et al., *Fluorescence resonance energy transfer microscopy as demonstrated by measuring the activation of the serine/threonine kinase Akt.* Nature protocols, 2013. **8**(2): p. 265.

4. Bottiroli, G., et al., *Autofluorescence spectroscopy of cells and tissues as a tool for biomedical diagnosis.* 2004. **3**(11-12): p. 189-210.

5. Croce, A.C. and G. Bottiroli, *Autofluorescence spectroscopy and imaging: a tool for biomedical research and diagnosis.* Eur J Histochem, 2014. **58**(4): p. 2461.

6. Garcia-Plazaola, J.I., et al., *Autofluorescence: Biological functions and technical applications.* Plant Sci, 2015. **236**: p. 136-45.

7. Gosnell, M.E., et al., *Functional hyperspectral imaging captures subtle details of cell metabolism in olfactory neurosphere cells, disease-specific models of neurodegenerative disorders.* Biochimica et Biophysica Acta (BBA)-Molecular Cell Research, 2016. **1863**(1): p. 56-63.

8. Gosnell, M.E., et al., *Quantitative non-invasive cell characterisation and discrimination based on multispectral autofluorescence features.* Sci Rep, 2016. **6**: p. 23453.

9. van Es, M.A., et al., *Amyotrophic lateral sclerosis.* Lancet, 2017. **390**(10107): p. 2084-2098.

10. Gordon, P.H., *Amyotrophic Lateral Sclerosis: An update for 2013 Clinical Features, Pathophysiology, Management and Therapeutic Trials.* Aging Dis, 2013. **4**(5): p. 295-310.

11. Brooks, B.R., et al., *El Escorial revisited: revised criteria for the diagnosis of amyotrophic lateral sclerosis.* Amyotroph Lateral Scler Other Motor Neuron Disord, 2000. **1**(5): p. 293-9.

12. Kabashi, E., et al., *TARDBP mutations in individuals with sporadic and familial amyotrophic lateral sclerosis.* Nat Genet, 2008. **40**(5): p. 572-4.

13. Mackenzie, I.R., R. Rademakers, and M. Neumann, *TDP-43 and FUS in amyotrophic lateral sclerosis and frontotemporal dementia.* Lancet Neurol, 2010. **9**(10): p. 995-1007.

14. Arnold, E.S., et al., *ALS-linked TDP-43 mutations produce aberrant RNA splicing and adult-onset motor neuron disease without aggregation or loss of nuclear TDP-43.* Proc Natl Acad Sci U S A, 2013. **110**(8): p. E736-45.

15. Sreedharan, J., et al., *Age-Dependent TDP-43-Mediated Motor Neuron Degeneration Requires GSK3, hat-trick, and xmas-2.* Curr Biol, 2015. **25**(16): p. 2130-6.

16. Banerjee, R., et al., *Adaptive immune neuroprotection in G93A-SOD1 amyotrophic lateral sclerosis mice.* PLoS One, 2008. **3**(7): p. e2740.

17. Geser, F., V.M. Lee, and J.Q. Trojanowski, *Amyotrophic lateral sclerosis and frontotemporal lobar degeneration: a spectrum of TDP-43 proteinopathies.* Neuropathology, 2010. **30**(2): p. 103-12.

18. Turner, M.R., et al., *Controversies and priorities in amyotrophic lateral sclerosis.* Lancet Neurol, 2013. **12**(3): p. 310-22.

19. Soo, K.Y., et al., *Rab1-dependent ER-Golgi transport dysfunction is a common pathogenic mechanism in SOD1, TDP-43 and FUS-associated ALS.* Acta Neuropathol, 2015. **130**(5): p. 679-97.

20. Al-Chalabi, A., L.H. van den Berg, and J. Veldink, *Gene discovery in amyotrophic lateral sclerosis: implications for clinical management.* Nat Rev Neurol, 2017. **13**(2): p. 96-104.

21. Shaw, P.J., *Molecular and cellular pathways of neurodegeneration in motor neurone disease.* J Neurol Neurosurg Psychiatry, 2005. **76**(8): p. 1046-57.

22. Goodall, E.F. and K.E. Morrison, *Amyotrophic lateral sclerosis (motor neuron disease): proposed mechanisms and pathways to treatment.* Expert Rev Mol Med, 2006. **8**(11): p. 1-22.

23. Pasinelli, P. and R.H. Brown, *Molecular biology of amyotrophic lateral sclerosis: insights from genetics.* Nat Rev Neurosci, 2006. **7**(9): p. 710-23.

24. Singh, R., et al., *Oxidative stress evokes a metabolic adaptation that favors increased NADPH synthesis and decreased NADH production in Pseudomonas fluorescens.* J Bacteriol, 2007. **189**(18): p. 6665-75.

25. Baumer, D., et al., *The role of RNA processing in the pathogenesis of motor neuron degeneration.* Expert Rev Mol Med, 2010. **12**: p. e21.

26. Duffy, L.M., et al., *Review: The role of mitochondria in the pathogenesis of amyotrophic lateral sclerosis.* Neuropathol Appl Neurobiol, 2011. **37**(4): p. 336-52.

27. Lee, E.B., V.M. Lee, and J.Q. Trojanowski, *Gains or losses: molecular mechanisms of TDP43-mediated neurodegeneration.* Nat Rev Neurosci, 2011. **13**(1): p. 38-50.

28. Shi, C. and E.G. Pamer, *Monocyte recruitment during infection and inflammation.* Nat Rev Immunol, 2011. **11**(11): p. 762-74.

29. Sheng, Z.H. and Q. Cai, *Mitochondrial transport in neurons: impact on synaptic homeostasis and neurodegeneration.* Nat Rev Neurosci, 2012. **13**(2): p. 77-93.

30. Turner, M.R., et al., *Mechanisms, models and biomarkers in amyotrophic lateral sclerosis.* Amyotroph Lateral Scler Frontotemporal Degener, 2013. **14 Suppl 1**(sup1): p. 19-32.

31. Paez-Colasante, X., et al., *Amyotrophic lateral sclerosis: mechanisms and therapeutics in the epigenomic era.* Nat Rev Neurol, 2015. **11**(5): p. 266-79.

32. Zarei, S., et al., *A comprehensive review of amyotrophic lateral sclerosis.* Surg Neurol Int, 2015. **6**: p. 171.

33. Morello, G., A.G. Spampinato, and S. Cavallaro, *Neuroinflammation and ALS: Transcriptomic Insights into Molecular Disease Mechanisms and Therapeutic Targets.* Mediators Inflamm, 2017. **2017**: p. 7070469.

34. Turner, M.R., et al., *Biomarkers in amyotrophic lateral sclerosis.* The Lancet Neurology, 2009. **8**(1): p. 94-109.

35. Bowser, R., M.R. Turner, and J. Shefner, *Biomarkers in amyotrophic lateral sclerosis: opportunities and limitations.* Nat Rev Neurol, 2011. **7**(11): p. 631-8.

36. Benatar, M., et al., *ALS biomarkers for therapy development: State of the field and future directions.* Muscle Nerve, 2016. **53**(2): p. 169-82.

37. Gowen, A.A., E. Gaston, and V. Valdramidis, *The Potential of Hyperspectral Imaging for Monitoring Microbial Activity in Foods.* Novel Food Preserv. and Microb. Assess. Techn, 2014. **435**.

38. Goetz, A.F., et al., *Imaging spectrometry for Earth remote sensing.* Science, 1985. **228**(4704): p. 1147-53.

39. Goetz, A.F.H., *Three decades of hyperspectral remote sensing of the Earth: A personal view.* Remote Sensing of Environment, 2009. **113**: p. S5-S16.

40. Li, Q., et al., *Review of spectral imaging technology in biomedical engineering: achievements and challenges.* J Biomed Opt, 2013. **18**(10): p. 100901.

41. Amigo, J.M., et al., *Study of pharmaceutical samples by NIR chemical-image and multivariate analysis.* TrAC - Trends in Analytical Chemistry, 2008. **27**(8): p. 696-713.

42. Gendrin, C., Y. Roggo, and C. Collet, *Pharmaceutical applications of vibrational chemical imaging and chemometrics: A review.* Journal of Pharmaceutical and Biomedical Analysis, 2008. **48**(3): p. 533-553.

43. Amigo, J.M., *Practical issues of hyperspectral imaging analysis of solid dosage forms.* Analytical and Bioanalytical Chemistry, 2010. **398**(1): p. 93-109.

44. Roggo, Y., et al., *Infrared hyperspectral imaging for qualitative analysis of pharmaceutical solid forms.* Analytica Chimica Acta, 2005. **535**(1-2): p. 79-87.

45. Ravn, C., E. Skibsted, and R. Bro, *Near-infrared chemical imaging (NIR-CI) on pharmaceutical solid dosage forms-Comparing common calibration approaches.* Journal of Pharmaceutical and Biomedical Analysis, 2008. **48**(3): p. 554-561.

46. Cruz, J., et al., *Nir-chemical imaging study of acetylsalicylic acid in commercial tablets.* Talanta, 2009. **80**(2): p. 473-478.

47. ElMasry, G., et al., *Principles and Applications of Hyperspectral Imaging in Quality Evaluation of Agro-Food Products: A Review.* Critical Reviews in Food Science and Nutrition, 2012. **52**(11): p. 999-1023.

48. ElMasry, G., et al., *Hyperspectral imaging for nondestructive determination of some quality attributes for strawberry.* Journal of Food Engineering, 2007. **81**(1): p. 98-107.

49. Mehl, P.M., et al., *Development of hyperspectral imaging technique for the detection of apple surface defects and contaminations.* Journal of Food Engineering, 2004. **61**(1 SPEC.): p. 67-81.

50. Cubero, S., et al., *Advances in Machine Vision Applications for Automatic Inspection and Quality Evaluation of Fruits and Vegetables.* Food and Bioprocess Technology, 2011. **4**(4): p. 487-504.

51. Gowen, A.A., et al., *Hyperspectral imaging - an emerging process analytical tool for food quality and safety control.* Trends in Food Science and Technology, 2007. **18**(12): p. 590-598.

52. Cheng, J.H. and D.W. Sun, *Hyperspectral imaging as an effective tool for quality analysis and control of fish and other seafoods: Current research and potential applications.* Trends in Food Science and Technology, 2014. **37**(2): p. 78-91.

53. Sun, D.W., *Hyperspectral Imaging for Food Quality Analysis and Control*. Hyperspectral Imaging for Food Quality Analysis and Control. 2010: Elsevier Inc.

54. Fernández Pierna, J.A., et al., *NIR hyperspectral imaging spectroscopy and chemometrics for the detection of undesirable substances in food and feed.* Chemometrics and Intelligent Laboratory Systems, 2012. **117**: p. 233-239.

55. Lorente, D., et al., *Recent Advances and Applications of Hyperspectral Imaging for Fruit and Vegetable Quality Assessment.* Food and Bioprocess Technology, 2012. **5**(4): p. 1121-1142.

56. Xiong, Z., et al., *Recent developments of hyperspectral imaging systems and their applications in detecting quality attributes of red meats: A review.* Journal of Food Engineering, 2014. **132**: p. 1-13.

57. Feng, Y.Z. and D.W. Sun, *Application of hyperspectral imaging in food safety inspection and control: a review.* Crit Rev Food Sci Nutr, 2012. **52**(11): p. 1039-58.

58. Flynn, K., et al., *Forensic applications of infrared chemical imaging: Multi-layered paint chips.* Journal of Forensic Sciences, 2005. **50**(4): p. 832-841.

59. Edelman, G.J., et al., *Hyperspectral imaging for non-contact analysis of forensic traces.* Forensic Sci Int, 2012. **223**(1-3): p. 28-39.

60. Schuler, R.L., P.E. Kish, and C.A. Plese, *Preliminary observations on the ability of hyperspectral imaging to provide detection and visualization of bloodstain patterns on black fabrics.* J Forensic Sci, 2012. **57**(6): p. 1562-9.

61. Carapezza, E.M., et al., *Using VIS/NIR and IR spectral cameras for detecting and separating crime scene details*, in *Sensors, and Command, Control, Communications, and Intelligence (C3I) Technologies for Homeland Security and Homeland Defense XI*. 2012. p. 83590P-83590P-11.

62. Kokaly, R.F., et al., *Characterizing canopy biochemistry from imaging spectroscopy and its application to ecosystem studies.* Remote Sensing of Environment, 2009. **113**(SUPPL. 1): p. S78-S91.

63. Weissleder, R. and M. Nahrendorf, *Advancing biomedical imaging.* Proc Natl Acad Sci U S A, 2015. **112**(47): p. 14424-8.

64. Lu, G. and B. Fei, *Medical hyperspectral imaging: a review.* J Biomed Opt, 2014. **19**(1): p. 10901.

65. Feng, Z., et al., *Multispectral Imaging of T and B Cells in Murine Spleen and Tumor.* J Immunol, 2016. **196**(9): p. 3943-50.

66. Gowen, A.A., et al., *Recent applications of hyperspectral imaging in microbiology.* Talanta, 2015. **137**: p. 43-54.

67. Klein, M.E., et al., *Quantitative hyperspectral reflectance imaging.* Sensors, 2008. **8**(9): p. 5576-5618.

68. Faigenbaum-Golovin, S., et al., *Multispectral imaging reveals biblical-period inscription unnoticed for half a century.* PLoS One, 2017. **12**(6): p. e0178400.

69. Staikopoulos, V., et al. *Hyperspectral imaging of endogenous fluorescent metabolic molecules to identify pain states in central nervous system tissue*. in *SPIE BioPhotonics Australasia*. 2016. International Society for Optics and Photonics.

70. Dobrucki, J.W. and U. Kubitscheck, *Fluorescence Microscopy*. 2017. 85-132.

71. Stockert, J.C. and A. Blazquez-Castro, *Fluorescence Microscopy in Life Sciences*. 2017: Bentham Science Publishers.

72. Liu, J.J., C. Liu, and W. He, *Fluorophores and Their Applications as Molecular Probes in Living Cells.* Current Organic Chemistry, 2013. **17**(6): p. 564-579.

73. Gispert, J.R., *Coordination chemistry*. Vol. 483. 2008: Wiley-VCH Weinheim.

74. Berezin, M.Y. and S. Achilefu, *Fluorescence lifetime measurements and biological imaging.* Chem Rev, 2010. **110**(5): p. 2641-84.

75. Zheng, W., et al., *Optimal excitation-emission wavelengths for autofluorescence diagnosis of bladder tumors.* Int J Cancer, 2003. **104**(4): p. 477-81.

76. Gupta, P.K., et al., *Breast cancer diagnosis using N2 laser excited autofluorescence spectroscopy.* 1997. **21**(5): p. 417-422.

77. Wizenty, J., et al., *Autofluorescence: A potential pitfall in immunofluorescence-based inflammation grading.* J Immunol Methods, 2018. **456**: p. 28-37.

78. Croce, A.C., et al., *Autofluorescence-based optical biopsy: An effective diagnostic tool in hepatology.* Liver Int, 2018. **38**(7): p. 1160-1174.

79. Periasamy, A., et al., *An automated image processing routine for segmentation of cell cytoplasms in high-resolution autofluorescence images*, in *Multiphoton Microscopy in the Biomedical Sciences XIV*. 2014.

80. Monici, M., *Cell and tissue autofluorescence research and diagnostic applications.* Biotechnol Annu Rev, 2005. **11**: p. 227-56.

81. Gosnell, M.E., et al., *Functional hyperspectral imaging captures subtle details of cell metabolism in olfactory neurosphere cells, disease-specific models of neurodegenerative disorders.* Biochim Biophys Acta, 2016. **1863**(1): p. 56-63.

82. Mansfield, J.R., *Multispectral imaging: a review of its technical aspects and applications in anatomic pathology.* Vet Pathol, 2014. **51**(1): p. 185-210.

83. Talamond, P., J.L. Verdeil, and G. Conejero, *Secondary metabolite localization by autofluorescence in living plant cells.* Molecules, 2015. **20**(3): p. 5024-37.

84. He, Q., et al., *Value of autofluorescence imaging videobronchoscopy in detecting lung cancers and precancerous lesions: a review.* Respir Care, 2013. **58**(12): p. 2150-9.

85. Levenson, R.M. and J.R. Mansfield, *Multispectral imaging in biology and medicine: slices of life.* Cytometry A, 2006. **69**(8): p. 748-58.

86. Skala, M.C., et al., *In vivo multiphoton microscopy of NADH and FAD redox states, fluorescence lifetimes, and cellular morphology in precancerous epithelia.* Proc Natl Acad Sci U S A, 2007. **104**(49): p. 19494-9.

87. Xu, H.N., et al., *Optical redox imaging indices discriminate human breast cancer from normal tissues.* J Biomed Opt, 2016. **21**(11): p. 114003.

88. Ostrander, J.H., et al., *Optical redox ratio differentiates breast cancer cell lines based on estrogen receptor status.* Cancer Res, 2010. **70**(11): p. 4759-66.

89. Alhallak, K., et al., *Optical redox ratio identifies metastatic potential-dependent changes in breast cancer cell metabolism.* Biomed Opt Express, 2016. **7**(11): p. 4364-4374.

90. Lichtman, J.W. and J.A. Conchello, *Fluorescence microscopy.* Nat Methods, 2005. **2**(12): p. 910-9.

91. Uckermann, O., et al., *Endogenous Two-Photon Excited Fluorescence Provides Label-Free Visualization of the Inflammatory Response in the Rodent Spinal Cord.* Biomed Res Int, 2015. **2015**: p. 859084.

92. Wessels, J.T., U. Pliquett, and F.S. Wouters, *Light-emitting diodes in modern microscopy--from David to Goliath?* Cytometry A, 2012. **81**(3): p. 188-97.

93. Aswani, K., T. Jinadasa, and C.M. Brown, *Fluorescence Microscopy Light Sources.* Microscopy Today, 2012. **20**(4): p. 22-28.

94. Combs, C.A. and H. Shroff, *Fluorescence Microscopy: A Concise Guide to Current Imaging Methods.* Curr Protoc Neurosci, 2017. **79**: p. 2 1 1-2 1 25.

95. Herman, B., *Fluorescence microscopy.* Curr Protoc Cell Biol, 2002. **Chapter 4**: p. Unit 4 2.

96. Herman, B., *Fluorescence microscopy.* Current protocols in cell biology, 1998(1): p. 4.2. 1-4.2. 10.

97. Dixit, R. and R. Cyr, *Cell damage and reactive oxygen species production induced by fluorescence microscopy: effect on mitosis and guidelines for non-invasive fluorescence microscopy.* Plant J, 2003. **36**(2): p. 280-90.

98. Kaludercic, N., S. Deshwal, and F. Di Lisa, *Reactive oxygen species and redox compartmentalization.* Frontiers in Physiology, 2014. **5**(285).

99. Gao, L. and R.T. Smith, *Optical hyperspectral imaging in microscopy and spectroscopy - a review of data acquisition.* J Biophotonics, 2015. **8**(6): p. 441-56.

100. Farley, V., et al., *Chemical agent detection and identification with a hyperspectral imaging infrared sensor*. Optics/Photonics in Security and Defence. Vol. 6739. 2007: SPIE.

101. Alivisatos, A.P., W. Gu, and C. Larabell, *Quantum dots as cellular probes.* Annu Rev Biomed Eng, 2005. **7**: p. 55-76.

102. Johnson, I. and M. Spencer, *The Molecular Probes R Handbook: A guide to fluorescent probes and labelling technologies. online: http://www. invitrogen. com/site/us/en/home/References/Molecular-Probes-The-Handbook/Fluorescent-Tracers-of-Cell-Morphology-and-Fluid-Flow/Tracers-for-Membrane-Labeling. html(as of 05/17/2011).* Carlsbad, CA: Invitrogen Corp.

103. Halimi, A., N. Dobigeon, and J.Y. Tourneret, *Unsupervised Unmixing of Hyperspectral Images Accounting for Endmember Variability.* IEEE Trans Image Process, 2015. **24**(12): p. 4904-17.

104. Goldman, D.B., *Vignette and exposure calibration and compensation.* IEEE transactions on pattern analysis and machine intelligence, 2010. **32**(12): p. 2276-2288.

105. Smith, K., et al., *CIDRE: an illumination-correction method for optical microscopy.* Nat Methods, 2015. **12**(5): p. 404-6.

106. Ngadi, M.O. and L. Liu, *Hyperspectral image processing techniques*, in *Hyperspectral imaging for food quality analysis and control*. 2010, Elsevier. p. 99-127.

107. Irie, K., et al., *A technique for evaluation of CCD video-camera noise.* Ieee Transactions on Circuits and Systems for Video Technology, 2008. **18**(2): p. 280-284.

108. Gosnell, M.E., *Unlocking the Potential of Spectral Imaging for the Characterisation of Cell and Stem Cell Populations*. 2014, Macquarie University, Faculty of Science, Department of Physics and Astronomy.

109. Goldys, E.M., et al. *Label-free multispectral imaging for biological research and medical diagnostics (Conference Presentation)*. in *Label-free Biomedical Imaging and Sensing (LBIS) 2019*. 2019. International Society for Optics and Photonics.

110. Nakamura, J., *Image sensors and signal processing for digital still cameras*. 2016: CRC press.

111. Healey, G.E. and R. Kondepudy, *Radiometric Ccd Camera Calibration and Noise Estimation.* Ieee Transactions on Pattern Analysis and Machine Intelligence, 1994. **16**(3): p. 267-276.

112. Lambert, T.J. and J.C. Waters, *Assessing camera performance for quantitative microscopy.* Methods Cell Biol, 2014. **123**: p. 35-53.

113. Robbins, M.S. and B.J. Hadwen, *The noise performance of electron multiplying charge-coupled devices.* Ieee Transactions on Electron Devices, 2003. **50**(5): p. 1227-1232.

114. Ruckebusch, C. and L. Blanchet, *Multivariate curve resolution: a review of advanced and tailored applications and challenges.* Anal Chim Acta, 2013. **765**: p. 28-36.

115. Saba, T., et al., *Evaluation of Current Documents Image Denoising Techniques: A Comparative Study.* Applied Artificial Intelligence, 2014. **28**(9): p. 879-887.

116. Waters, J.C. and T. Wittmann, *Concepts in quantitative fluorescence microscopy.* Methods Cell Biol, 2014. **123**: p. 1-18.

117. Rehman, A.U., et al., *Fluorescence quenching of free and bound NADH in HeLa cells determined by hyperspectral imaging and unmixing of cell autofluorescence.* Biomed Opt Express, 2017. **8**(3): p. 1488-1498.

118. Amigo, J.M., H. Babamoradi, and S. Elcoroaristizabal, *Hyperspectral image analysis. A tutorial.* Anal Chim Acta, 2015. **896**: p. 34-51.

119. Yoon, S.-C. and B. Park, *Hyperspectral Image Processing Methods*, in *Hyperspectral Imaging Technology in Food and Agriculture*, B. Park and R. Lu, Editors. 2015, Springer New York: New York, NY. p. 81-101.

120. Hummel, R., *Image enhancement by histogram transformation.* Unknown, 1975.

121. Maini, R. and H. Aggarwal, *A comprehensive review of image enhancement techniques.* arXiv preprint arXiv:1003.4053, 2010.

122. Bedi, S. and R. Khandelwal, *Various image enhancement techniques-a critical review.* International Journal of Advanced Research in Computer and Communication Engineering, 2013. **2**(3).

123. Siddiqi, A.M., et al., *Use of hyperspectral imaging to distinguish normal, precancerous, and cancerous cells.* Cancer Cytopathology: Interdisciplinary International Journal of the American Cancer Society, 2008. **114**(1): p. 13-21.

124. Greenman, R.L., et al., *Early changes in the skin microcirculation and muscle metabolism of the diabetic foot.* The Lancet, 2005. **366**(9498): p. 1711-1717.

125. Freeman, J.E., et al., *Hyperspectral imaging in diabetes and peripheral vascular disease*. 2013, Google Patents.

126. Mahbub, S.B., et al., *Non-Invasive Monitoring of Functional State of Articular Cartilage Tissue with Label-Free Unsupervised Hyperspectral Imaging.* Sci Rep, 2019. **9**(1): p. 4398.

127. Pu, Y., et al., *Native fluorescence spectra of human cancerous and normal breast tissues analyzed with non-negative constraint methods.* Appl Opt, 2013. **52**(6): p. 1293-301.

128. Wang, L. and C. Zhao, *Hyperspectral Image Processing*. 2016: Springer.

129. Roman, G.C., *Neuroepidemiology of amyotrophic lateral sclerosis: clues to aetiology and pathogenesis.* Journal of neurology, neurosurgery, and psychiatry, 1996. **61**(2): p. 131.

130. Festoff, B.W., *Erratum to Amyotrophic lateral sclerosis: current and future treatment strategies.* Drugs, 2012. **52**(1): p. 92-92.

131. Kinsley L, S.T. .*Amyotrophic Lateral Sclerosis Overview.* GeneReviews® [Internet]. 2001 Mar 23 2015 Feb 12 [cited 2019; Available from: https://www.ncbi.nlm.nih.gov/books/NBK1450/.

132. Ioannides, Z.A., et al., *Altered Metabolic Homeostasis in Amyotrophic Lateral Sclerosis: Mechanisms of Energy Imbalance and Contribution to Disease Progression.* Neurodegener Dis, 2016. **16**(5-6): p. 382-97.

133. Bensimon, G., et al., *A controlled trial of riluzole in amyotrophic lateral sclerosis.* New England Journal of Medicine, 1994. **330**(9): p. 585-591.

134. Al-Chalabi, A., et al., *Amyotrophic lateral sclerosis: moving towards a new classification system.* Lancet Neurol, 2016. **15**(11): p. 1182-94.

135. Yedavalli, V.S., A. Patil, and P. Shah, *Amyotrophic Lateral Sclerosis and its Mimics/Variants: A Comprehensive Review.* J Clin Imaging Sci, 2018. **8**: p. 53.

136. Tiryaki, E. and H.A. Horak, *ALS and other motor neuron diseases.* Continuum (Minneap Minn), 2014. **20**(5 Peripheral Nervous System Disorders): p. 1185-207.

137. Boylan, K., et al., *Immunoreactivity of the phosphorylated axonal neurofilament H subunit (pNF‐H) in blood of ALS model rodents and ALS patients: evaluation of blood pNF‐H as a potential ALS biomarker.* Journal of neurochemistry, 2009. **111**(5): p. 1182-1191.

138. Mitchell, R., et al., *A CSF biomarker panel for identification of patients with amyotrophic lateral sclerosis.* Neurology, 2009. **72**(1): p. 14-19.

139. Nardo, G., et al., *Amyotrophic lateral sclerosis multiprotein biomarkers in peripheral blood mononuclear cells.* PloS one, 2011. **6**(10): p. e25545.

140. Shepheard, S.R., et al., *Urinary p75ECD: A prognostic, disease progression, and pharmacodynamic biomarker in ALS.* Neurology, 2017. **88**(12): p. 1137-1143.

141. Simpson, E., et al., *Increased lipid peroxidation in sera of ALS patients: a potential biomarker of disease burden.* Neurology, 2004. **62**(10): p. 1758-1765.

142. Swindell, W.R., et al., *ALS blood expression profiling identifies new biomarkers, patient subgroups, and evidence for neutrophilia and hypoxia.* J Transl Med, 2019. **17**(1): p. 170.

143. Brettschneider, J., et al., *Axonal damage markers in cerebrospinal fluid are increased in ALS.* Neurology, 2006. **66**(6): p. 852-856.

144. Süssmuth, S., et al., *CSF glial markers correlate with survival in amyotrophic lateral sclerosis.* Neurology, 2010. **74**(12): p. 982-987.

145. Kuhle, J., et al., *Increased levels of inflammatory chemokines in amyotrophic lateral sclerosis.* European journal of neurology, 2009. **16**(6): p. 771-774.

146. Neumann, M., et al., *Ubiquitinated TDP-43 in frontotemporal lobar degeneration and amyotrophic lateral sclerosis.* Science, 2006. **314**(5796): p. 130-133.

147. Bowling, A.C., et al., *Superoxide dismutase activity, oxidative damage, and mitochondrial energy metabolism in familial and sporadic amyotrophic lateral sclerosis.* Journal of neurochemistry, 1993. **61**(6): p. 2322-2325.

148. Sreedharan, J., et al., *TDP-43 mutations in familial and sporadic amyotrophic lateral sclerosis.* Science, 2008. **319**(5870): p. 1668-1672.

149. Vance, M.L., *Cushing's disease: radiation therapy.* Pituitary, 2009. **12**(1): p. 11.

150. Keizman, D., et al., *Low uric acid levels in serum of patients with ALS: further evidence for oxidative stress?* Journal of the neurological sciences, 2009. **285**(1-2): p. 95-99.

151. Whitwell, J.L., *Voxel-based morphometry: an automated technique for assessing structural changes in the brain.* J Neurosci, 2009. **29**(31): p. 9661-4.

152. Menke, R.A.L., et al., *Widespread grey matter pathology dominates the longitudinal cerebral MRI and clinical landscape of amyotrophic lateral sclerosis.* Brain : a journal of neurology, 2014. **137**(Pt 9): p. 2546-2555.

153. Chen, Z. and L. Ma, *Grey matter volume changes over the whole brain in amyotrophic lateral sclerosis: A voxel-wise meta-analysis of voxel based morphometry studies.* Amyotrophic Lateral Sclerosis, 2010. **11**(6): p. 549-554.

154. Le Bihan, D., et al., *Diffusion tensor imaging: concepts and applications.* Journal of Magnetic Resonance Imaging: An Official Journal of the International Society for Magnetic Resonance in Medicine, 2001. **13**(4): p. 534-546.

155. Dalakas, M.C., et al., *Lowered cerebral glucose utilization in amyotrophic lateral sclerosis.* Annals of Neurology: Official Journal of the American Neurological Association and the Child Neurology Society, 1987. **22**(5): p. 580-586.

156. Brown, A.K., et al., *Radiation dosimetry and biodistribution in monkey and man of 11C-PBR28: a PET radioligand to image inflammation.* Journal of Nuclear Medicine, 2007. **48**(12): p. 2072-2079.

157. Kimura, J., *Electrodiagnosis in diseases of nerve and muscle: principles and practice*. 2013: Oxford university press.

158. Swash, M. and M. de Carvalho, *The neurophysiological index in ALS.* Amyotrophic Lateral Sclerosis and Other Motor Neuron Disorders, 2004. **5**(sup1): p. 108-110.

159. McComas, A., et al., *Electrophysiological estimation of the number of motor units within a human muscle.* Journal of Neurology, Neurosurgery & Psychiatry, 1971. **34**(2): p. 121-131.

160. Pare, B. and F. Gros-Louis, *Potential skin involvement in ALS: revisiting Charcot's observation–a review of skin abnormalities in ALS.* Reviews in the Neurosciences, 2017. **28**(5): p. 551-572.

161. Shepheard, S.R., et al., *The extracellular domain of neurotrophin receptor p75 as a candidate biomarker for amyotrophic lateral sclerosis.* PLoS One, 2014. **9**(1): p. e87398.

162. Moloney, E.B., F. de Winter, and J. Verhaagen, *ALS as a distal axonopathy: molecular mechanisms affecting neuromuscular junction stability in the presymptomatic stages of the disease.* Front Neurosci, 2014. **8**: p. 252.

163. Liu, Z., et al., *Oxidative Stress in Neurodegenerative Diseases: From Molecular Mechanisms to Clinical Applications.* Oxid Med Cell Longev, 2017. **2017**: p. 2525967.

164. Rothstein, J.D., et al., *Abnormal excitatory amino acid metabolism in amyotrophic lateral sclerosis.* Annals of neurology, 1990. **28**(1): p. 18-25.

165. Spreux-Varoquaux, O., et al., *Glutamate levels in cerebrospinal fluid in amyotrophic lateral sclerosis: a reappraisal using a new HPLC method with*

coulometric detection in a large cohort of patients. Journal of the neurological sciences, 2002. **193**(2): p. 73-78.

166. Rothstein, J.D., et al., *Selective loss of glial glutamate transporter GLT ‐ 1 in amyotrophic lateral sclerosis.* Annals of Neurology: Official Journal of the American Neurological Association and the Child Neurology Society, 1995. **38**(1): p. 73-84.

167. Rothstein, J.D., et al., *β-Lactam antibiotics offer neuroprotection by increasing glutamate transporter expression.* Nature, 2005. **433**(7021): p. 73.

168. Guo, H., et al., *Increased expression of the glial glutamate transporter EAAT2 modulates excitotoxicity and delays the onset but not the outcome of ALS in mice.* Human molecular genetics, 2003. **12**(19): p. 2519-2532.

169. Doble, A., *The pharmacology and mechanism of action of riluzole.* Neurology, 1996. **47**(6 Suppl 4): p. 233S-241S.

170. Magrané, J. and G. Manfredi, *Mitochondrial function, morphology, and axonal transport in amyotrophic lateral sclerosis.* Antioxidants & redox signaling, 2009. **11**(7): p. 1615-1626.

171. Kawamata, H. and G. Manfredi, *Mitochondrial dysfunction and intracellular calcium dysregulation in ALS.* Mechanisms of ageing and development, 2010. **131**(7-8): p. 517-526.

172. Dupuis, L., et al., *Evidence for defective energy homeostasis in amyotrophic lateral sclerosis: benefit of a high-energy diet in a transgenic mouse model.* Proceedings of the National Academy of Sciences, 2004. **101**(30): p. 11159-11164.

173. Dupuis, L., et al., *Energy metabolism in amyotrophic lateral sclerosis.* The Lancet Neurology, 2011. **10**(1): p. 75-82.

174. Dupuis, L., et al., *Dyslipidemia is a protective factor in amyotrophic lateral sclerosis.* Neurology, 2008. **70**(13): p. 1004-1009.

175. Chiò, A., et al., *Lower serum lipid levels are related to respiratory impairment in patients with ALS.* Neurology, 2009. **73**(20): p. 1681-1685.

176. Dorst, J., et al., *Patients with elevated triglyceride and cholesterol serum levels have a prolonged survival in amyotrophic lateral sclerosis.* Journal of neurology, 2011. **258**(4): p. 613-617.

177. Lawton, K.A., et al., *Biochemical alterations associated with ALS.* Amyotrophic Lateral Sclerosis, 2012. **13**(1): p. 110-118.

178. Sies, H., *Biochemistry of oxidative stress.* Angewandte Chemie International Edition in English, 1986. **25**(12): p. 1058-1071.

179. Sies, H., *Oxidative stress: From basic research to clinical application.* The American Journal of Medicine, 1991. **91**(3): p. S31-S38.

180. D'Amico, E., et al., *Clinical perspective on oxidative stress in sporadic amyotrophic lateral sclerosis.* Free Radic Biol Med, 2013. **65**: p. 509-527.

181. Cookson, M.R. and P.J. Shaw, *Oxidative Stress and Motor Neurone Disease.* Brain Pathology, 2006. **9**(1): p. 165-186.

182. Tu, P., et al., *Oxidative stress, mutant SOD1, and neurofilament pathology in transgenic mouse models of human motor neuron disease.* Laboratory investigation; a journal of technical methods and pathology, 1997. **76**(4): p. 441-456.

183. Tang, A.Y., *RNA-binding proteins associated molecular mechanisms of motor neuron degeneration pathogenesis.* Mol Biotechnol, 2014. **56**(9): p. 779-86.

184. Philips, T. and W. Robberecht, *Neuroinflammation in amyotrophic lateral sclerosis: role of glial activation in motor neuron disease.* Lancet Neurol, 2011. **10**(3): p. 253-63.

185. Bruijn, L.I., T.M. Miller, and D.W. Cleveland, *Unraveling the mechanisms involved in motor neuron degeneration in ALS.* Annu Rev Neurosci, 2004. **27**: p. 723-49.

186. Brown, G.C. and A. Vilalta, *How microglia kill neurons.* Brain Res, 2015. **1628**(Pt B): p. 288-297.

187. Dong, Y. and E.N. Benveniste, *Immune function of astrocytes.* Glia, 2001. **36**(2): p. 180-190.

188. Baufeld, C., et al., *Differential contribution of microglia and monocytes in neurodegenerative diseases.* J Neural Transm (Vienna), 2018. **125**(5): p. 809-826.

189. Streit, W.J., R.E. Mrak, and W.S.T. Griffin, *Microglia and neuroinflammation: a pathological perspective.* Journal of neuroinflammation, 2004. **1**(1): p. 14.

190. Lehnardt, S., *Innate immunity and neuroinflammation in the CNS: The role of microglia in Toll‐like receptor‐mediated neuronal injury.* Glia, 2010. **58**(3): p. 253-263.

191. Chan, W.Y., S. Kohsaka, and P. Rezaie, *The origin and cell lineage of microglia: new concepts.* Brain Res Rev, 2007. **53**(2): p. 344-54.

192. Zhang, R., et al., *Evidence for systemic immune system alterations in sporadic amyotrophic lateral sclerosis (sALS).* Journal of neuroimmunology, 2005. **159**(1-2): p. 215-224.

193. Zhang, R., et al., *MCP-1 chemokine receptor CCR2 is decreased on circulating monocytes in sporadic amyotrophic lateral sclerosis (sALS).* Journal of neuroimmunology, 2006. **179**(1-2): p. 87-93.

194. Butovsky, O., et al., *Modulating inflammatory monocytes with a unique microRNA gene signature ameliorates murine ALS.* The Journal of clinical investigation, 2012. **122**(9): p. 3063-3087.

195. Zhao, W., et al., *Characterization of gene expression phenotype in amyotrophic lateral sclerosis monocytes.* JAMA neurology, 2017. **74**(6): p. 677-685.

196. Zondler, L., et al., *Peripheral monocytes are functionally altered and invade the CNS in ALS patients.* Acta neuropathologica, 2016. **132**(3): p. 391-411.

197. Jakubzick, C.V., G.J. Randolph, and P.M. Henson, *Monocyte differentiation and antigen-presenting functions.* Nat Rev Immunol, 2017. **17**(6): p. 349-362.

198. Hettinger, J., et al., *Origin of monocytes and macrophages in a committed progenitor.* Nature immunology, 2013. **14**(8): p. 821.

199. Mildner, A., et al., *Microglia in the adult brain arise from Ly-6C hi CCR2+ monocytes only under defined host conditions.* Nature neuroscience, 2007. **10**(12): p. 1544.

200. Kho, E., et al., *Hyperspectral Imaging for Resection Margin Assessment during Cancer Surgery.* Clin Cancer Res, 2019. **25**(12): p. 3572-3580.

201. Baltussen, E.J.M., et al., *Hyperspectral imaging for tissue classification, a way toward smart laparoscopic colorectal surgery.* J Biomed Opt, 2019. **24**(1): p. 1-9.

202. Morris, J.D. and C.K. Payne, *Microscopy and Cell Biology: New Methods and New Questions.* Annu Rev Phys Chem, 2019. **70**: p. 199-218.

203. Olympus. *IX71/IX81 - Olympus - Life Science*. 2016; Available from: https://www.olympus-lifescience.com/data/olympusmicro/brochures/pdfs/ix71.pdf?rev=EABE.

204. Andor, *iXon+885+specification*.

205. Verrier, N. and M. Atlan, *Absolute measurement of small-amplitude vibrations by time-averaged heterodyne holography with a dual local oscillator.* Opt Lett, 2013. **38**(5): p. 739-41.

206. Sivaguru, M., et al., *Comparative performance of airyscan and structured illumination superresolution microscopy in the study of the surface texture and 3D shape of pollen.* Microsc Res Tech, 2018. **81**(2): p. 101-114.

207. Moraru, C. and R. Amann, *Crystal ball: fluorescence in situ hybridization in the age of super-resolution microscopy.* Syst Appl Microbiol, 2012. **35**(8): p. 549-52.

208. Huang, W., et al., *The effect of excess expression of GFP in a novel heart-specific green fluorescence zebrafish regulated by nppa enhancer at early embryonic development.* Mol Biol Rep, 2011. **38**(2): p. 793-9.

209. Long, F., S. Zeng, and Z.L. Huang, *Localization-based super-resolution microscopy with an sCMOS camera part II: experimental methodology for comparing sCMOS with EMCCD cameras.* Opt Express, 2012. **20**(16): p. 17741-59.

210. Herzog, N., M. Shein-Idelson, and Y. Hanein, *Optical validation of in vitro extra-cellular neuronal recordings.* J Neural Eng, 2011. **8**(5): p. 056008.

211. Ahola, A., et al., *Simultaneous Measurement of Contraction and Calcium Transients in Stem Cell Derived Cardiomyocytes.* Ann Biomed Eng, 2018. **46**(1): p. 148-158.

212. LLC, C.E.G. *Catalog number: Gbd00004-200*. 2016; Available from: http://celleg.com/product/product4.html.

213. North, A.J., *Seeing is believing? A beginners' guide to practical pitfalls in image acquisition.* The Journal of cell biology, 2006. **172**(1): p. 9-18.

214. Mahbub, S.B., et al., *Statistically strong label-free quantitative identification of native fluorophores in a biological sample.* Sci Rep, 2017. **7**(1): p. 15792.

215. Bhatta, H. and E.M. Goldys, *Quantitative characterization of different strains of Saccharomyces yeast by analysis of fluorescence microscopy images of cell populations.* J Microbiol Methods, 2009. **77**(1): p. 77-84.

216. Stangenberg, S., et al., *Oxidative stress, mitochondrial perturbations and fetal programming of renal disease induced by maternal smoking.* Int J Biochem Cell Biol, 2015. **64**: p. 81-90.

217. Jolliffe, I.T. and J. Cadima, *Principal component analysis: a review and recent developments.* Philos Trans A Math Phys Eng Sci, 2016. **374**(2065): p. 20150202.

218. Liuzzi, V.C., et al., *Silencing of FAD synthase gene in Caenorhabditis elegans upsets protein homeostasis and impacts on complex behavioral patterns.* Biochimica Et Biophysica Acta (BBA)-General Subjects, 2012. **1820**(4): p. 521-531.

219. Parakh, S., et al., *Redox regulation in amyotrophic lateral sclerosis.* Oxid Med Cell Longev, 2013. **2013**: p. 408681.

220. Huhner, J., et al., *Quantification of riboflavin, flavin mononucleotide, and flavin adenine dinucleotide in mammalian model cells by CE with LED-induced fluorescence detection.* Electrophoresis, 2015. **36**(4): p. 518-25.

Appendix

A. The single Channel analysis result

The following figures are single-channel analysis results for each channel for all samples.

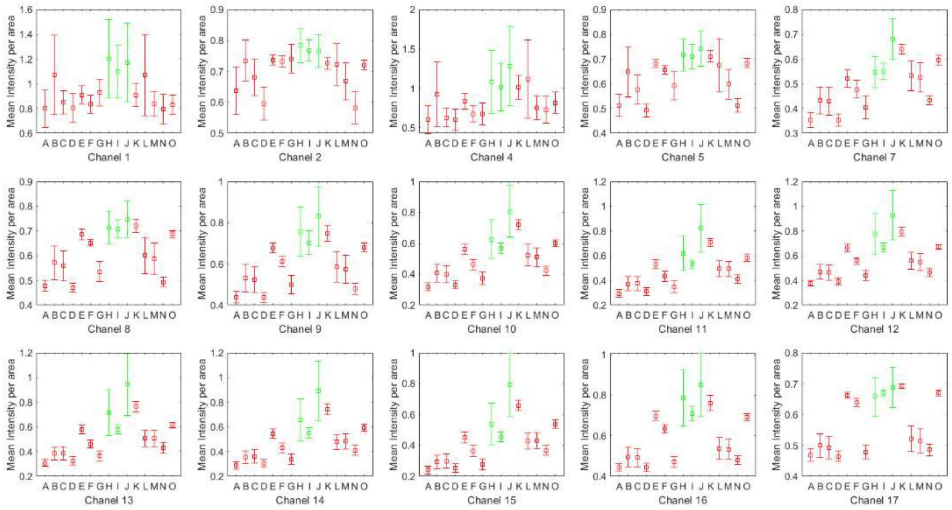

Figure A-1 single-channel analysis for channel 15

B. Supplement result for LDA

Table A-1 shows a summary of misclassified observations for the classification attempt by principal component 1 and 2

Table B-1 Linear Discriminant Function for Groups

Observation	True Group	Predict Group	Group	Squared Distance	Probability
K	P	C	C	3.984	0.541
			P	4.315	0.459
L	P	C	C	2.595	0.828
			P	5.741	0.172

C. HSI image processing tool

The following **Figure C-1** shows the control panel of my HSI image processing tool.

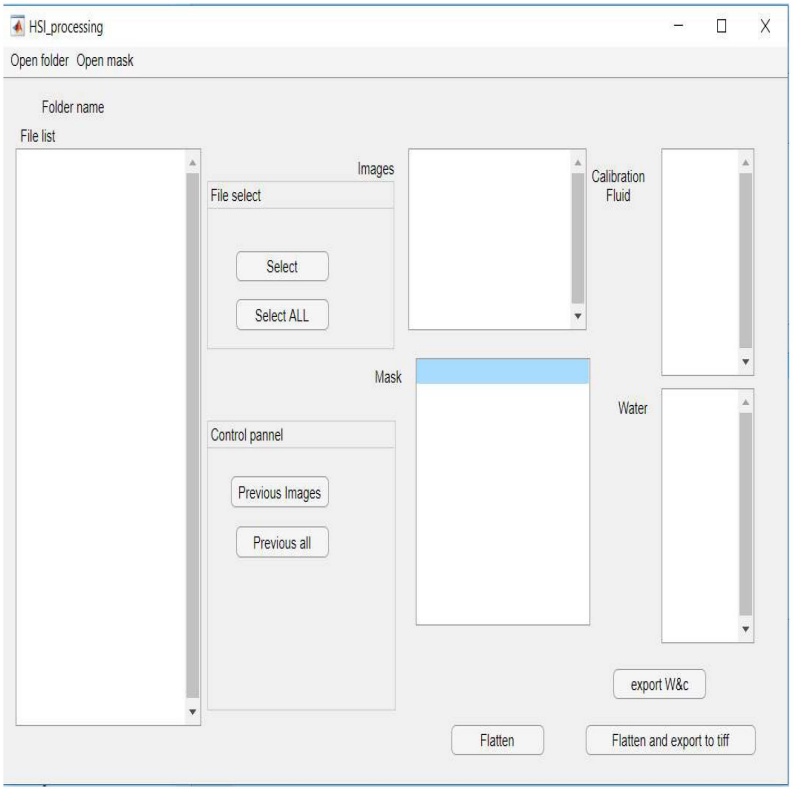

Figure B-1 Control pannel of HSI processing app

The functions of this tool include the following:

- Previous of HSI sample images, water, and calibration fluid images
- PPS conversion for HSI images.
- Apply median filter on HSI images for spikes removal
- Smoothing of water and calibration fluid
- Flattening of HSI image.
- Final image smoothing.

D. Sample code

The following Table D-1 is the table for the group of each sample(patient and control) with related patient codes.

Table D-1 Sample states and cell number measured

Sample code	Status	Cell number
A	Patient	**72**
B	Patient	151
C	Patient	49
D	Patient	71
E	Patient	73
F	Patient	91
G	Patient	98
H	Control	104
I	Control	367
J	Control	118
K	Patient	79
L	Patient	143
M	Patient	50
N	Patient	65
O	Patient	92

E. Camera specification

Table E-1 EMCCD camera specification

Specifications	Values
Active Pixels	1004 × 1002
Image Area (µm)	200 × 200
Active Area Pixel Well Depth (e-, typical)	30,000
Gain Register pixel well depth (e-, typical):	80,000
Max Readout Rate (MHz)	35

Frame Rate at full resolution at 31.4 at 2 × 2 binning	60.5
Read Noise (e-, typical)	- 25 @ 35 MHZ, with EM Gain less than 1 - 22 @ 27 MHZ, with EM, Gain less than 1 - 12 @ 13 MHZ, with EM, Gain less than 1
Sensitivity (electrons per digital count) @max pre-gain of 3.7	- 1.23 at a readout rate of 35 MHz - 1.27 at a readout rate of 22 MHz - 0.89 at a readout rate of 13 MHz
Quantum Efficiency (%): 65 @ 602 nm	Detail graph is presented in **Figure 3-5**(b)
Pixel Readout Rate (MHz)	35, 27, 13 MHz
Linearity (% deviation from line up to maximum)	1%
Vertical Clock Speed μs)	0.5,1, 1.9, 3.4
Electron Multiplier Gain	1 - 1000 times (software controlled) via RealGain™control, temperature compensation and linearity correction
Digitization @ 35, 27 & 13 MHz readout rate	14-bit
Air-cooled (ambient air at 20℃)	-70℃
Dark Current @ -85℃ (e-/pix/sec)	0.002

F. Using data acquisition GUI to take images

In the MATLAB command window, this data acquisition GUI runs by writing the command of spectralControllerGUI.

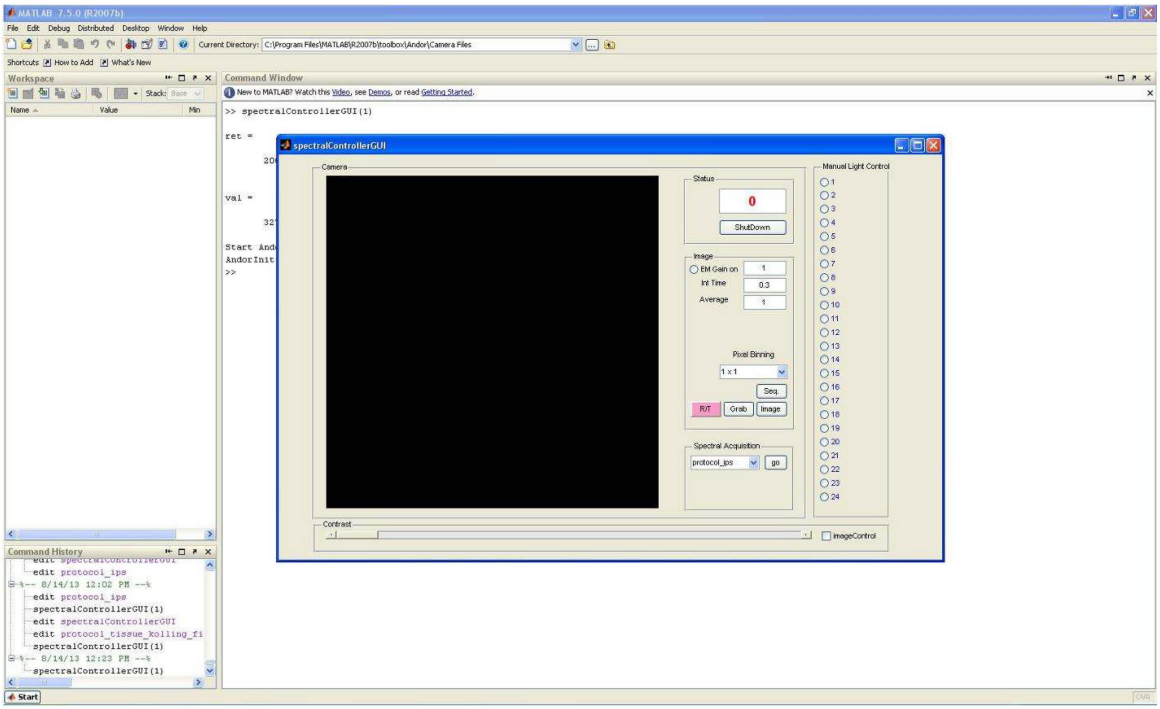

Figure F-1 spectralControllerGUI runs through the MATLAB platform.

Then it will open a popup window after a few seconds, which is actually taking control over the EMCCD and LED bank of the HS system. **Figure F-1** shows the spectralControllerGUI window.

It is crucial to cool down the EMCCDs sensors to reduce the background noises. As manufacturers specification, the preferable working temperature for EMCCD is below -65°C. A GUI interface window (denoting by the A in **Figure F-2**), it shows the real-time temperature. Moreover, This GUI has strictly maintained the prerequisite of -60°C, and beyond this temperature, the user cannot start or perform any experiments. It will take around 2-5 minutes to cool down at -65°C concerning room temperature and previous usages.

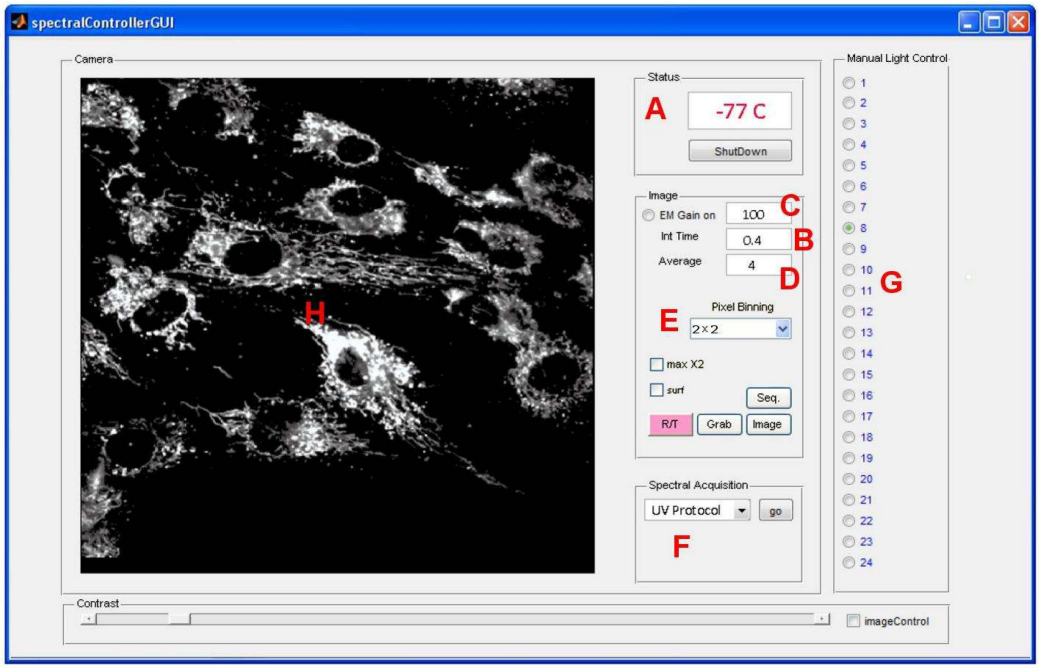

Figure F-2 spectralControllerGUI platform with panel notations.

Figure F-2, `A', highlights the different input panels. A denotes the real-time temperature for the EMCCD camera. Whereas, `B' takes the excitation duration in seconds, and `C' receives the EM gain from the user. Furthermore, the `D' panel takes the averaging counts for the experiment. All these three parameters are based upon a specific channel with a particular cell line. `H' panel is an output monitor that shows the image in real-time. This panel can be managed by the inputs specified in the pixel binning section `E.' Here `real-time (R/T)' switch enables the continuous mode.

Furthermore, `grab' and `image' options are used for saving an image at the specific channel. It is crucial that to deactivate the real-time session during software automated imaging sessions. Otherwise, data will not save or capture accurately. This window shows the sensor data (maximum, mean) over the entire area (around 200 μm × 200 μm) with digital counts. `max ×2' and `surf' option at `E' shows the smoothed surface image. This option allows for finding any sudden changes in the samples. This is very useful to take the calibration fluid to avoid any grid line or floating dirt. It also gives a better knowledge of the Gaussian distribution of the LED source around the center. `Pixel binning' will help us to focus on the very noisy situation by binning the total area by 2 ×2 or 4 ×4. However, during software automated imaging sessions, the binning is always set for 1 ×1 to get the maximum amount of information without any software-oriented smoothness. From the section `F,'

predefined user functions are chosen as a protocol file during software automated imaging sessions. After starting the automatic acquisition program, the software will prompt the filter number. At this stage, the user needs to check the appropriate filter physically and need to be careful about the unwanted light sources. After finishing with the first filter, a double beep tone notifies the user about changing the following filters. During DIC image acquisition, the corresponding message notifies as `filter no 0'. Normally filter no 1 (most of the cases) is used for DIC image, depending upon the image SNR during the protocol preparation. Moreover, at this stage, the predefined amount of microscope light is used for imaging.

Also, a description file is used to record the details of EM gain, exposer duration, and the quantum efficiency of the camera sensor for every image. SpectralControllerGUI saves a description file as `paramDesc xxxx.mat', Where xxxx is the user-defined file name. All the data are stacked under the struct variable, `para,' where data, time, protocol, imageSettings, stats, precise temperature are recorded. Within this struct, imageSettings saves the EM gain (as emGain), exposer duration (as emInt), averaging (as avg), excitation wavelength (as ex), emission wavelength (as em) and filter no (as filt). As an example, during the pre-processing, EM gain value can be called by the para.imageSettings (1,2).emGain. Nevertheless, it is crucial to synchronize the description file with the HS data cube for further use.

G. Biosafety approval

MACQUARIE University

SECTION A	Biohazard Risk Assessment Form – NON GMO		
		Notification Number:	*EWG021115BHA*

Chief Investigator :	**Ewa Goldys**	**Date:**	02/11/2015
Department:	**Physics and Astronomy Centre of Excellence for Nanoscale Biophotonics (ARC)**	**Contact number/email:**	
Title of research or practical	Advanced sensing and imaging of biological samples		

Exact location(s) of research: E7B 111, E7B 113, E7B106, F7B0

Are additional approvals required? ☐ **Animal Ethics** ☐ **Human Ethics** ☐ **Fieldwork** ☐ **Other (please state)**

Control measures:

☐ **Eliminate risk** ☐ **Substitute the hazard** ☒ **Isolate the hazard** ☐ **Implement engineering controls** ☒ **Administration (e.g. SWP/Training** ☒ **PPE**

E.g. eliminated by irradiation prior to use, isolation by class II biological safety cabinets, administration by following SWP as below, PPE as listed below.

Supporting documents which must be read in conjunction with this assessment. (e.g. Safe Working Procedures, Safety Data Sheets, Guidelines/Protocols)

Previous Approval (5201100537LAB), Biohazard Approval *(AAN300412BHA)*

What is the type of the biological material?

☐ **Bacteria** ☐ **Fungus** ☐ **Virus** ☒ **Cell Line** ☒ **Tissue** ☐ **Parasite**

☐ **Animal** ☐ **Plant** ☐ **Soil** ☐ **Toxins** ☐ **Prions** ☐ **Nucleic Acid** ☐ **Other** _____

What is the name of the biological agent?

Primary cell lines from ATCC, cell lines derived from human, Tissues from Human and Mice(Frozen), Fluids from Human and animals.

Personal Protective Equipment required:

☒ **Gloves** *(e.g. chemical resistant)* ☒ **Clothing** *(e.g. button up lab coat/coveralls/apron)* ☐ **Respiratory Protection** *(e.g.PF2 face mask)*

☒ **Eye protection** *(e.g. safety glasses/goggles)* ☒ **Footwear** *(e.g. Enclosed/Gumboots/overshoe covers)* ☐ **Other** _____

H. Ethic approval

MACQUARIE University

Macquarie University
Neurodegenerative Disease Biobank
Project Request Form

Faculty of Medicine & Health Sciences
F10A Building
2 Technology Place
Macquarie University,
NSW 2109,
Australia

Date of Request:

Project Title: Hyperspectral characterization of peripheral blood lymphocytes from ALS patients.

A. Investigator Information

Principle Investigator Name	Dominic Rowe/Gilles Guillemin

Contact Name	Ewa Goldys &Ayad Anwer
Contact Email	
Contact Phone	

Additional Investigator Name	Affiliation
Dominic B. Rowe	Professor of Neurology/ Faculty of Medicine and Health Sciences
Gilles Guillemin	MND Centre
Benjamin Heng	MND Centre
Ayad Anwer	Research associate and lab manager / Centre for Nanoscale BioPhotonics
Meng He	PhD student/ Centre for Nanoscale BioPhotonics
Abbas Habibalahi	PhD student/Centre for Nanoscale BioPhotonics

Add extra lines as required

B. Research Project

1. Project Approval

Biobank Project Number *(include if amending existing application, otherwise for committee use)*	DR001
Biobank HREC Number	5201600387
External Affiliation Ethics Details	
Grant information and Number	